EFFECT OF CRYSTALLOGRAPHY ON STRESS CORROSION CRACKING GROWTH IN AUSTENITIC STAINLESS STEELS

by

Haozheng J. Qu

A Thesis

Submitted to the Faculty of Purdue University

In Partial Fulfillment of the Requirements for the degree of

Master of Science in Industrial Engineering

School of Industrial Engineering

West Lafayette, Indiana

December 2020

THE PURDUE UNIVERSITY GRADUATE SCHOOL
STATEMENT OF COMMITTEE APPROVAL

Dr. Janelle P. Wharry, Co-Chair

School of Materials Engineering

Dr. Gary J. Cheng, Co-Chair

School of Industrial Engineering

Dr. Wenzhuo Wu

School of Industrial Engineering

Approved by:

Dr. Abhijit Deshmukh

Soli Deo Gloria

ACKNOWLEDGMENTS

First and foremost, I would like to give my greatest gratitude to my advisor, Dr. Janelle P. Wharry, for her unconditional support and encouragement throughout my master's program. Without her gracious care, wise guidance and everlasting patience, especially during the hardest period of my life, there is no chance for me to make it through my master's degree and forward as a life-long learner. Her hard word, dedication and mentorship inspired me to push through roadblocks academically and mentally. I wish one day I can encourage and help others as well as she can.

I want to thank my co-chair, Dr. Gary J. Cheng, for his gracious support by giving me the precious opportunity to pursue academic excellence at Purdue University. I also wish to thank Dr. Wenzhuo Wu for his service on my dissertation committee.

During this journey, my fellows in our loving group have also provided strong support and very useful discussions: Dr. Kayla Yano, Dr. Keyou Mao, Priyam Patki, Amrita Sen, Patrick Warren, George Warren, Caleb Clement, Yangyang Zhao and Chao Yang. I am exceedingly blessed with the brotherhood with Keyou for his encouragement during hard periods and constructive discussions on both faith and experiments. I want to extend my appreciation to mentors and staff at Sandia National Laboratory for their support on the corrosion tests: Dr. Eric J. Schindelholz (Now at Ohio State University), Dr. Rebecca Schaller and Timothy Montoya.

There is no word that could ever express my deepest love to my parents. It's the scars on their hands and the sweat on their faces that built the stairs for me to come abroad to explore the new world and shape who I am here at Purdue University. Mom and dad, thank you for being my dearest parents and I will never forget your sacrifice for me.

I was nineteen when I came to the United States, not knowing who I truly am and what I am meant to do. I am grateful there were so many mentors, teachers and friends that helped me to grow and know who I am. Among all of them, I wish to give special thanks to my life mentor for their guidance and love that directed me to the love of Jesus Christ: Nicholas & Lydia Romanin and Peter & Mary Zhou. Their wisdom and love ignited the way I view myself and the world around me.

Finally, I would like very much to dedicate my appreciation to beloved Meng. Without your love, wisdom, patience, forgiveness, and care, there is no way for me become a man like today. Meng, thank you for sharing the joys and tears along this destined adventure with me.

This research was sponsored by the US Department of Energy Office of Nuclear Energy award DE-NE0008759.

PREFACE

The image of stress corrosion I see
Is that of a huge unwanted tree
Against whose trunk we chop and chop,
But which outgrows the chips that drop;
And from each gash made in its bark
A new branch grows to make more dark
The shade of ignorance around its base,
Where scientists toil with puzzled face.
(S. P. Rideout, 1967)[1]

TABLE OF CONTENTS

LIST OF TABLES

LIST OF FIGURES

ABBREVIATIONS

ASTM	American Society for Testing and Materials
UNM	University Of New Mexico
SCC	Stress Corrosion Cracking
FEA	Finite Element Analysis
HAZ	Heat Affected Zone
MPa	Megapascal
SEM	Scanning Electron Microscope
SE	secondary electron
BSE	backscattered electron
EBSD	Electron Backscatter Diffraction
GB	grain boundary
XRD	X-ray Diffraction Crystallography
FCC	face centered cubic
SS	stainless steel

ABSTRACT

Chloride induced stress corrosion cracking (CISCC) is one of the most vulnerable weaknesses for the widely used austenitic stainless steel in many industries. The complex nature of CISCC involves mechanical, electrochemical, and microstructural perspectives. The objective of this thesis is to assess CISCC phenomenon in austenitic stainless steel from the mechanical and crystallographic perspective, specifically on the effect of local strain and stress and anisotropic plastic deformation. Austenitic stainless steel 304L test coupons are bent in four-point bending fixtures to obtain tensile stress for CISCC, followed by corrosion experiment in boiling magnesium chloride solution. Stress state of the sample is evaluated by finite element analysis (FEA) and X-ray Diffraction Crystallography (XRD) prior corrosion test. Cross section of the cracked region are analyzed with Electron Backscatter Diffraction (EBSD) to analyze the relationship between CISCC behaviors and crystallographic features in the sample. Schmid factor and Taylor factor are used to quantitatively evaluate CISCC initiation and propagation behavior. It is learned that in polycrystalline FCC stainless steel, mismatch of Schmid factor and Taylor factor values in adjacent grains along crack path governs CISCC propagation susceptibility and path selection. Crack propagation factor competition model is proposed based on observations from EBSD maps, incorporating Schmid factor and Taylor factor mismatch, electrochemical condition of crack tip, and anisotropic properties.

1. INTRODUCTION

Austenitic stainless steel is one of the most commonly used materials for structural application in marine, defence, aerospace and nuclear industries due its high corrosion resistance. However, the one factor that limits extended application of austenitic stainless steel is its susceptibility to chloride induced stress corrosion cracking (CISCC) [2].

One of the most significant concerns raised in recent decade that drew tremendous attention to SCC susceptibility of austenitic stainless steels is spent nuclear fuel canister failure. There are currently more than a hundred operating nuclear reactors in the United States, many of which have been in operation for multiple decades [3]. During the routine operation of these nuclear power plants, spent nuclear fuel must be removed from the reactors and replaced with new fuel. The spent fuels are initially stored in spent fuel pools. However, as the spent fuel pools are reaching capacity, independent dry storage canisters were licensed by nuclear regulatory commission for additional storage capacity. Right now, there are over 2000 dry canisters in service and stored in separate concrete overpacks for radiation shielding [4]. According to the spent fuel storage concept, the decay heat of spent nuclear fuels dissipates through the canister wall by air cooling. Thus, the canister wall is in direct contact with moist air containing salt particles and suffers from chloride-induced stress corrosion cracking (SCC) from the deliquesces of deposited sea salts [5]. The Nuclear Regulatory Commission (NRC) normally provides 20 years initial license for the facilities to use dry canisters storage and part of the reason. As the initial license for most canisters are now approaching its end, many facilities are applying for license extension. But the problem for the safety evaluation is that it is almost impossible to take the canister out of the concrete overpack for inspection and repair because of the high radiation level. And also current regulations prohibit transportation of canisters with even particle cracks because of safety. Thus, solving the SCC problem of these dry canisters is critical and urgent nowadays.

SCC phenomena has a long history that dates back to the early twentieth century, leading to many explosion of steam engine boilers and it was also serious problem in the failure of firearms during both world wars [6]. The expensive failures of various systems have drawn a great scientific exploration on the topic since then. But well rounded theoretical mechanisms

were not proposed until 1950s and even after another 70 years of study, scientists have not arrived at a universally agreed theory to explain the mechanisms of how the three factors work to induce SCC. In the recent two decades, SCC research has been divided into more specialized factors controlling SCC phenomena. The objective of this thesis to assess CISCC initiation and propagation in austenitic stainless steel from a mechanical and crystallographic perspective.

2. BACKGROUND

2.1 Stress Corrosion Cracking (SCC)

2.1.1 Introduction

SCC is a type of Environmentally induced Cracking (EIC) that describes the growth of brittle cracks due to the simultaneous action of a stress (nominally static and tensile) and a reactive environment [7][8][9][10]. The susceptibility is further influenced by the rate of solution renewal, oxide rupture, and passivation at the crack tip as shown in Figure 2.2 [11]. Within the EIC family, SCC is often distinguished from fatigue corrosion by constant or monotonically increasing loading condition versus cyclic loading [12][13]. Typical characteristics of SCC include [6][14][15]:

1. Normally ductile alloys in inert environment usually fracture and fail in a brittle manner.

2. highly corrosion resistant alloys are very susceptible to SCC when stress exists (e.g. stainless steel is almost immune to boiling $MgCl_2$, but is highly susceptible to TGSCC when tensile stress exists).

3. Cracks are highly localized in transgranular (TG) or intergranular (IG) form, branched and usually perpendicular to the stress direction.

4. SCC is also an electrochemical process and resistance of SCC depends on alloy composition and electrode potential.

5. SCC behavior shows strong dependence on microstructure and surface condition.

6. SCC environment is different for different alloy.

2.1.2 Models for SCC mechanisms

Over the past century, there have been various universal models attempted to explain SCC phenomena, but even though many of them may apply to particular systems, they are not universally applicable to every environment-alloy combination [16][17][7][18][19]. Here is

a brief summary of past models proposed and how they are developed and evolved over the years.

Film Rupture Model

Film rupture mechanism (FRM) is the one of the oldest SCC mechanisms proposed by Mears [20] first in 1944 and confirmed by Logan [21] later in 1952.

When the stress is high enough, protective film will be broken by plastic deformation and the fresh exposed metal will become electronegative with respect to the filmed region. If such exposed material is connected to filmed areas by a conducting liquid, e.g., drops of liquid containing dissolved gases or salts, a short-circuited electrolytic cell will generate [20]. As the size of the film-free region is generally very small compared with the filmed area, the current density over the anodic film-free area is high, and corrosion will proceed at a rapid rate until a readjustment of stresses permits repassivation. Stress corrosion will thus proceed along alternative paths until the stress concentration at the particular path under consideration becomes sufficient to rupture the protective film again [20].

Logan's report agrees generally with the "film rupture mechanism" idea proposed by Mears, his result shows that only minor plastic deformation is needed for film to rupture and expose film-free substrate, rather than tearing of the underlying metal [21]. In summary, Logan's FRM model is that SCC is caused by repetitive electrolytic reaction between film-free (anodic) substrate and passive film (cathodic) when stress is sufficient to rupture the passive film. Local stress will be adjusted based on the dissolution of the metal and when film reformation condition is satisfied, the dissolution reaction will become repetitive.

In 1972, Vermilyea outlined the prediction of crack propagation rate based on Logan's FRM model while assuming homogeneous metal [22]. Vermilyea quantified the crack growth to creep strain between film rupture and repassivation. The model he proposed is:

$$\dot{l} = \frac{L}{t_c} \tag{2.1}$$

where $\dot{l}$ is the rate of crack propagation, L is the metal loss depth of each film-rupture cycle, and t_c is the time between repassivation and new film rupture at critical strain $\dot{\varepsilon}$.

Slip-Dissolution Model

The conceptual mechanism of film rupture model was not experimentally validated until 1988 by Andreson and Ford [23]. Their model assumed Faraday's $2nd$ law governed the oxidation reactions (dissolution, repassivation and corrosion advance) that led to crack advancement at crack tip after film rupture, as shown in Figure 2.3. The protective film was ruptured repetitively by increasing strain in the underlying metal, when film fracture strain was reached[24]. The periodicity t_f can be calculated based on the fracture strain of the passive film and strain rate at crack tip. The growth rate of the model was summarized in a general form [23]:

$$(\frac{da}{dt}) = f(n)(\frac{d\varepsilon}{dt})^n_{ct} \tag{2.2}$$

where $(\frac{da}{dt})$ is the crack growth rate, n is a parameter representing environment and material chemistry effect on oxidation, and $(\frac{d\varepsilon}{dt})^n_{ct}$ is the crack tip strain rate.

The environmental and chemical factor f(n) is later correlated to oxidation/repassivation current density i(n) as [25][26]:

$$f(n) = (\frac{M}{z\rho F})\mathrm{i}(n)dt \tag{2.3}$$

where: M is the metal's atomic weight, z is the valence state, ρ is density, and F is Faraday' s constant. The oxidation/repassivation current density i(n) decays exponentially with time t.

Smith and Staehle gave a good demonstration of how slip step initiates local dissolution in Figure 2.4 [27][28].

To distinguish characteristics of SCC under this model, Visualisation of surface topography, pitting, surface dissolution and formation of a passive film, can be measured directly [29].

Film-induced Cleavage Model

Film-induced cleavage model was first proposed by Edeleanu and Forty to explain the sudden and discontinuous appearance of crack traces during brittle fracture in the α-brass immersed in ammonia solution [30]. Based on their optical microscopic observation of the crack, repetitive brittle cracking is triggered by selective dezincification and embrittlement on surface, propagated freely until halted at slip band. Their observation of discontinuous cracks was later confirmed in scanning electron microscope (SEM) by Beavers and Pugh [31]. Beavers and Pugh also illustrated the model schematically, as shown in figure 2.6 [9]. Their results showed that cracks propagated on {011} planes, rather than {111}, with surface steps on $(1\bar{1}1)$ and $(11\bar{1})$ alternatively. The fact that step faces were {111} slips planes indicated that steps were formed by shear rather than tearing. The discontinuity of the crack indicated that crack tip must be completely re-passivated, rather than continuously disarrayed by elastic strain, before subsequent rupture and propagation.

Modern film-induced cleavage models were advanced by Newman and Sieradzki from both mechanistic and electrochemical perspectives. They concluded that dealloyed or oxidized thin films must be involved with crack initiation based on the crack advance event (AE) acoustic frequency they reported [32]. The active path along which the crack propagates is cyclically generated as film disruption and rebuild alternate with each other, and propagation is controlled by the slip characteristics of the substrate metal. This strain-generated active path mechanism typically leads transgranular cracking [33].

Corrosion Enhanced Plasticity Model (CEPM)

Magnin proposed the corrosion enhanced plasticity model (CEPM) in 1996 [34][35], and subsequently reviewed by Chateau in 2002 [36][37]. CEPM tries to explain the zig-zag micro-fracture along alternating {111} slip planes of austenitic stainless steels in Cl^- solutions. In this model, local fracture occurs in the enhanced plasticity region from the formation of dislocation pile-up along slip-planes. When pile-up is hindered by obstacles, like Lomer–Cottrell locks, local stress is severely intensified and leads to decohesion. In the presence of hydro-

gen at crack tip, local cohesion energy is further decreased and decohesion is eased [36]. Schematic illustration of Magnin's CEPM model is shown in Figure 2.5 [35].

2.1.3 Controversy

There are many more models proposed over the years assessing various alloys in different environments. Yet, the above four models are main focus studying CISCC of austenitic stainless steels [14][2]. Among these four models, there is controversy between continuous (slip dissolution) and discontinuous (CEPM) TGSCC mechanism, depending on the final fractography. Zhu builds another comprehensive model with continuous major cracking from anodic dissolution and discontinuous secondary cracking from local fracture (fractography shows river pattern) [38]

Although under a particular testing condition one mechanism may be valid, an alteration of the system variables could lead to operation of a different mechanism. Indeed, two or more mechanisms may be operating simultaneously.

2.2 Effect of Various Factors on SCC Phenomena

Mechanical, environmental and metallurgical factors have been shown to relate to CISCC growth [11][15][39]. Staehle has done an excellent job summarizing the empirical relationship between SCC depth and various factors, as shown in Figure 2.1 [40]. Effect of different factors will be discussed based on past literature below.

2.2.1 Mechanical Factors

TGSCC has been shown to be driven by localized deformation with environmental corrosion assistance [41][42]

Stress Intensity Factor

The applied stress intensity (K) is a function of the uniform stress and the crack length [43]:

$$K = \sigma\sqrt{\pi a} f(a) \tag{2.4}$$

where σ is macroscopic flow stress, a is crack length, and f(a) is dimensional factor. For a constant-stress test, the stress intensity increases as crack propagates longer. For low-strength materials, higher K leads to a significant plastic zone ahead of the crack tip [11].

2.2.2 Microstructural Factors

Phase Transformation

For austenitic stainless steels, like 304 and 316, Martensite transformation tends to be induced by plastic strain along grain boundaries and facilitated by hydrogen permeation [2]. For IGSCC, martensite at grain boundaries are specifically responsible for hydrogen embrittlement because of its high hydrogen diffusivity and permeability nature [44][2]. Mechanically, strain-induced martensite transformation leads to work-hardening and causes higher susceptibility to SCC as dissolution rate of martensite is much higher than austenite [45].

Grain Size Effect

Grain boundary has higher energies and thus is more chemically active [15]. Higher density of grain boundaries increases the reactivity of the surface through increased electron activity and diffusion. Besides, SCC typically involves electrochemical competition between passivation–repassivation kinetics of passive film formation and hydrogen diffusivity in the matrix, which is responsible for hydrogen-assisted SCC failure [46]. Increased surface reactivity coupled with more sites for oxide film nucleation of grain-refined materials lead to more rapid formation of protective layers [47][48], which will protect the crack path from blunting and induce rapid brittle cracking. In addition, electron work function (EWF) decreases with decreased grain size. Reduced atom coordination causes a surface to have a lower work function, which eases electron removal and adsorption of corrosion species [49]. Faster diffusion of hydrogen along grain boundaries can drive the crack propagation and cause accelerated failure in materials with finer grain [46].

Stacking Fault Energy (SFE)

Stacking Fault Energy (SFE) significant affects slip, twinning and ϵ-martensite transformation during deformation in FCC structure system [50][51][52]. In regard of deformation behavior, SFE value is divided into three categories:

1. SFE $> 50\ mJ/m^2$: plasticity dominated by slip
2. 15-18 $mJ/m^2 <$ SFE $< 50\ mJ/m^2$: plasticity dominated by twinning and slip
3. SFE $<$ 15-18 mJ/m^2: plasticity dominated by ϵ-martensite and slip.

Austenitic stainless steel 304 has low ($< 20mJ/m^2$) SFE at temperature below 100K and moderate (20-45 mJ/m^2) SFE at temperature between 100 and 300 K [53][54]. In this moderate range of SFE, twin nucleation and growth are eased because of dissociation preference of perfect dislocation. Besides, easier dissociation inhibit cross-slip and induces more dislocation pile-ups against obstacles [50], which assists SCC growth.

2.2.3 Environmental Factors

Hydrostatic Energy

Hydrogen diffusion and adsorption increase local energy that decrease stress required for crack to propagate [37]. Hydrogen segregation in the hydrostatic stress field of edge dislocations and the resulting asymmetric stress relaxation on the slip plane will decrease resolved shear stress, which is related to dislocations having a non-zero edge component [55]. This hydrostatic interaction between hydrogen and dislocations are referred as "hydrogen softening" that ease the stress cracking [36].

Temperature

The fracture type for SS304 in boiling Magnesium Chloride solution is reported to be transgranular at higher temperature (416K or higher) and intergranualar at lower temperature (408K) [2]. As temperature increases, both hydrogen absorption and escape rate increase whereas the amount of hydrogen entry decreases, leading to a overall decrease of

hydrogen entry. [56]. On the other hand, as test temperature increases, the dissolution rate of metallic substrate increases. At high temperature, when dissolution rate is higher than hydrogen entry rate, TGSCC will dominate over IGSCC [2].

Meisnar et.al [57] used transmission Kikuchi diffraction to study the tip chemistry and effect of temperature on crack growth rate in SS316 under PWR primary water environment. It was discovered that crack growth rate increases with temperature increase in the range of 250C - 320C, but decreases with temperature at higher temperature up to 360C. Higher oxidation and diffusion rate was attributed to the positive correlation between CGR and temperature.

2.3 Schmid Factor and Taylor Factor

Schmid factor is the direct parameter that determines the shear stress required to activate the most active slip system, assuming isostress equilibrium [58], as shown in Equation 2.3 [59].

$$\sigma_y = \frac{\tau_{CRSS}}{m}$$
$$m = cos\phi \cdot cos\lambda$$

where σ_y is yield strength of the grain, and τ_{CRSS} is the critical resolved shear stress on the active slip plane. High Schmid factor indicates less stress is required to provide sufficient shear stress on the active slip system [59]. Grains with high Schmid factor are oriented with easy slip step to break passive film to initiate brittle cracking across GB [7][60][27].

On the contrary, Taylor factor is derived based on the assumption of isostrain condition in polycrystalline [58]. It is typically used to correlate macroscopic flow stress and the resolved shear stress, assuming multiple slip systems share same shear stress as alternative to each other [61].

$$\sigma_x d\epsilon_x = \tau d\gamma$$
$$M = \frac{d\gamma}{d\epsilon_x} = \frac{\sigma_x}{\tau}$$

where σ is the macroscopic flow stress, ϵ is the grain strain, γ is the shear strain on each slip plane, and τ is the shear stress on active slip planes.

Low Taylor factor indicates that less shear strain is required to accommodate the overall tensile strain [62]. Thus, crack propagation is facilitated with reduced dislocation pile-up and localized strain at the grain boundary before a grain with low M. Meanwhile, because of the isostrain assumption, Taylor factor can also be used to evaluate grain specific stress in terms of macroscopic stress, as demonstrated in Equation 2.5.

$$\sigma_{hkl} = \frac{M_{hkl}}{M_{average}} \cdot \sigma_{average} \tag{2.5}$$

where σ_{hkl} is grain specific stress, M_{hkl} is the Taylor factor of the grain, and $M_{average}$ is the average Taylor factor for the randomly oriented sample, which is 3.067 for FCC polycrystalline as calculated by Taylor [59]. Grains with high Taylor factor experience higher stress than its surroundings, leading to more strain hardening and higher dislocation density to maintain strain compatibility with the neighbouring grains [63][59][64].

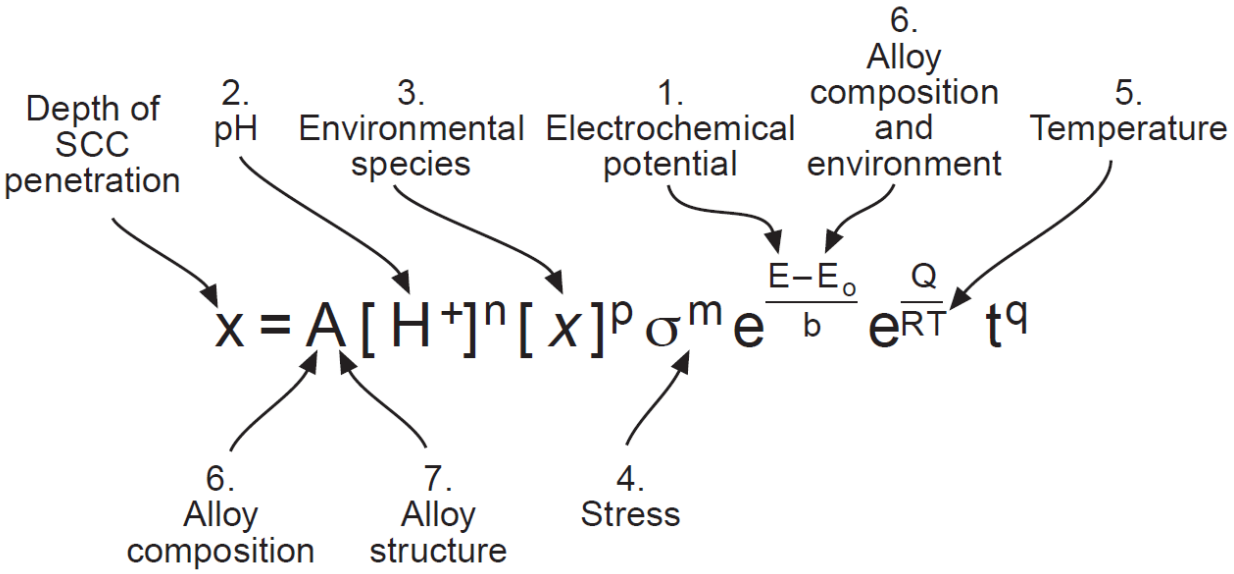

Figure 2.1. Generalized correlation of various factors with SCC penetration depth

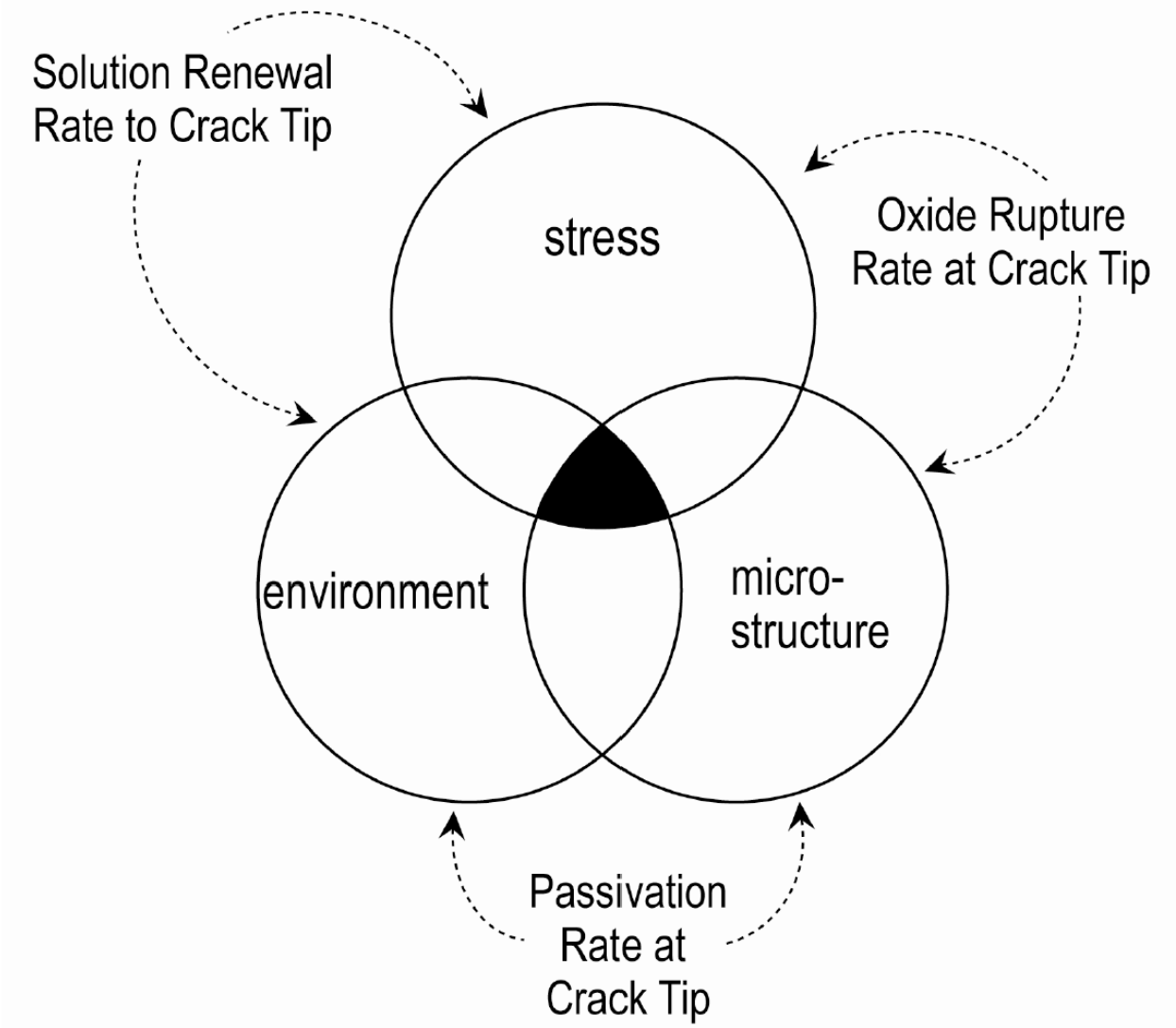

Figure 2.2. Schematic illustration of the interdependence of environmental, metallurgical, and stress conditions required for stress corrosion cracking [11]

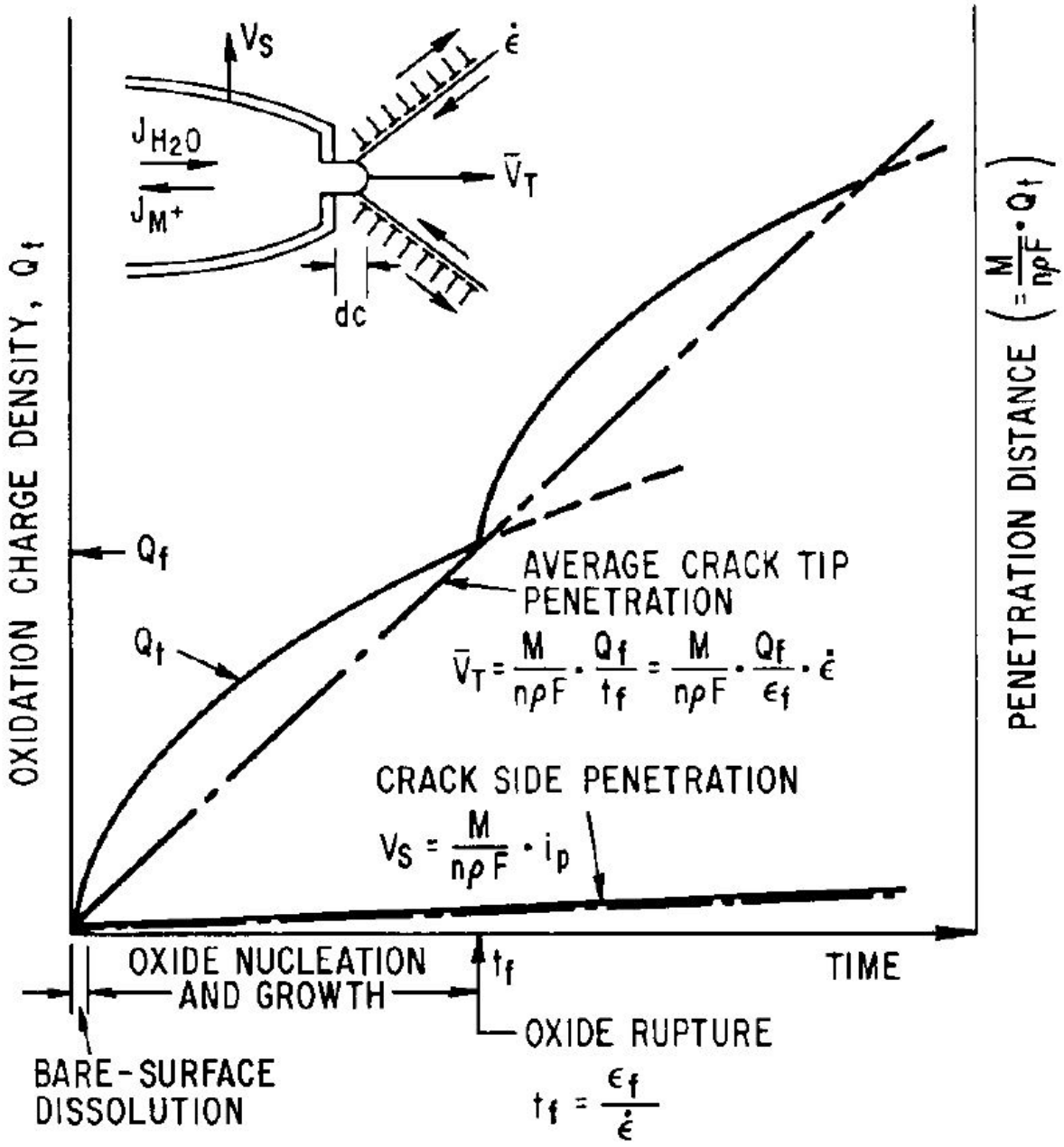

Figure 2.3. Illustration of oxidation charge density versus time for a strained crack tip

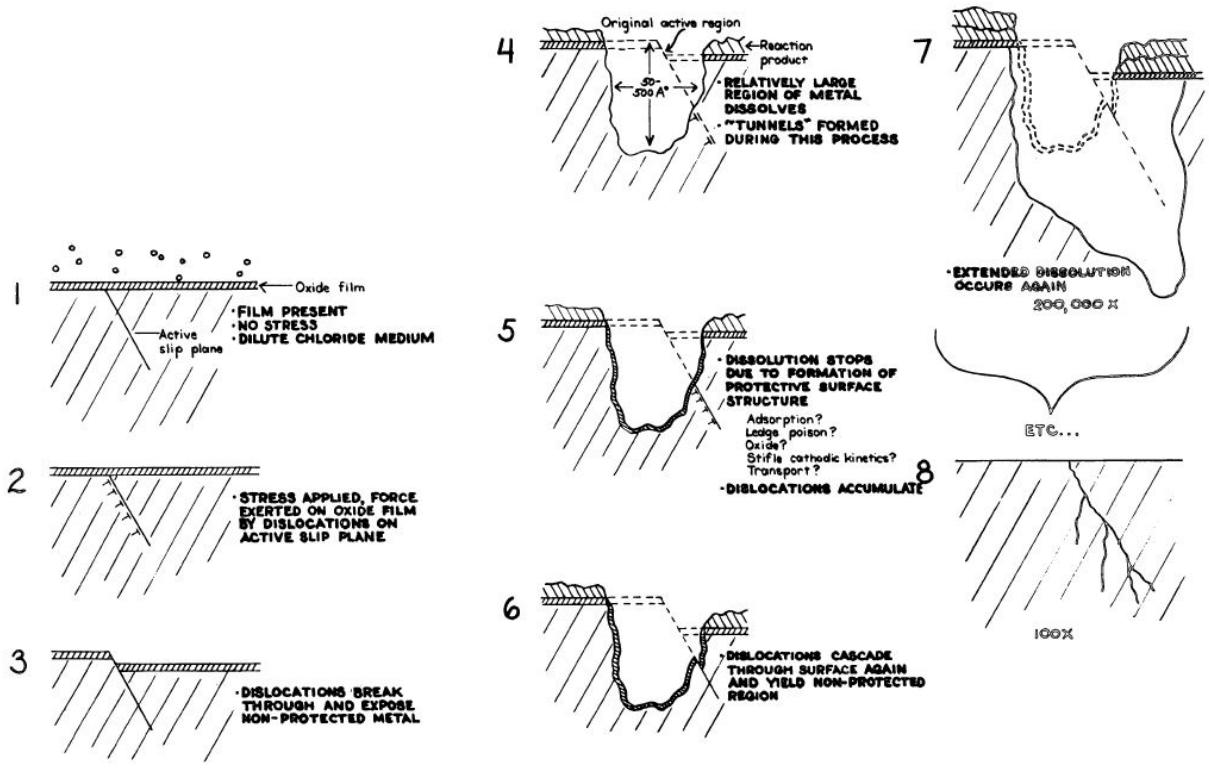

Figure 2.4. Schematic illustration of slip dissolution model for crack initiation and propagation [27]

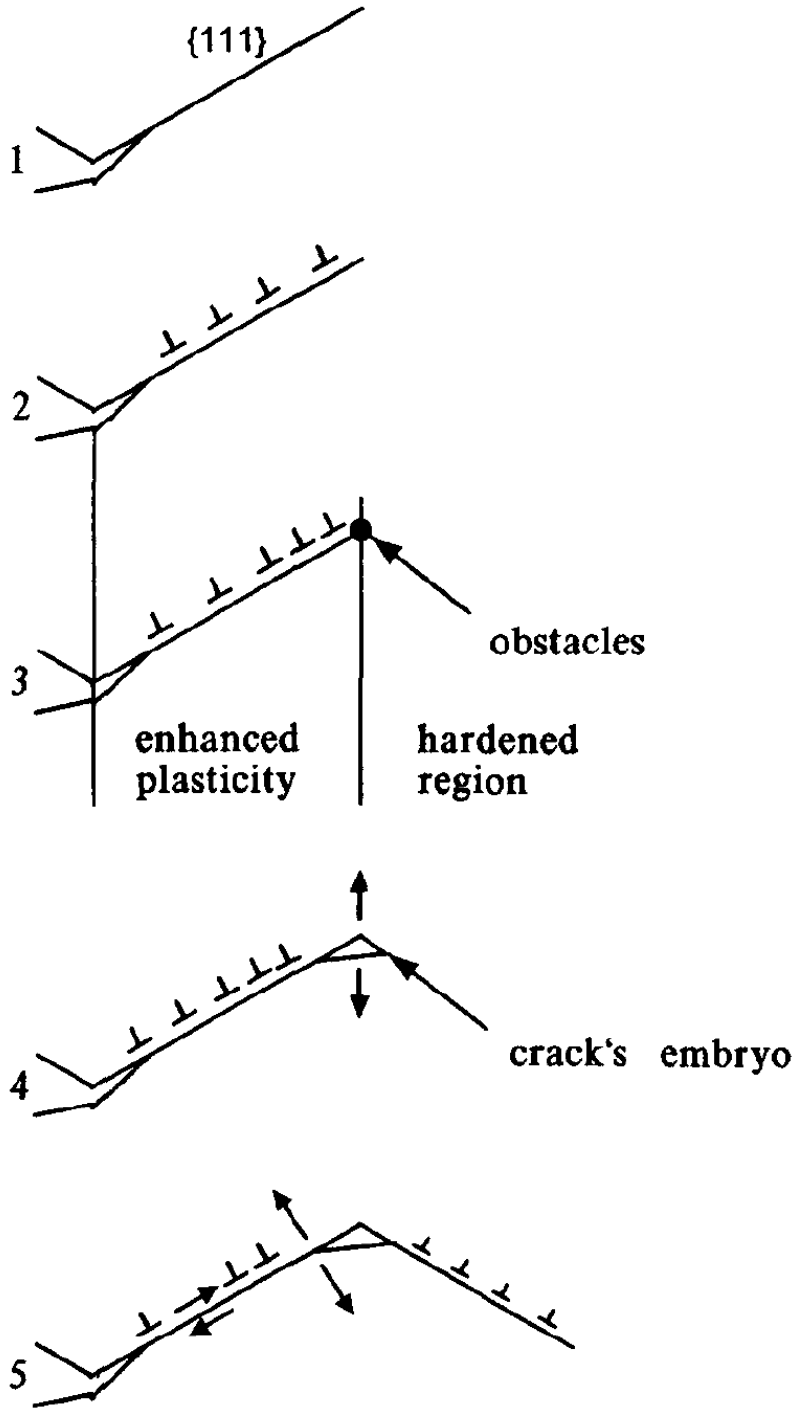

Figure 2.5. Schematic illustration of corrosion enhanced plasticity model

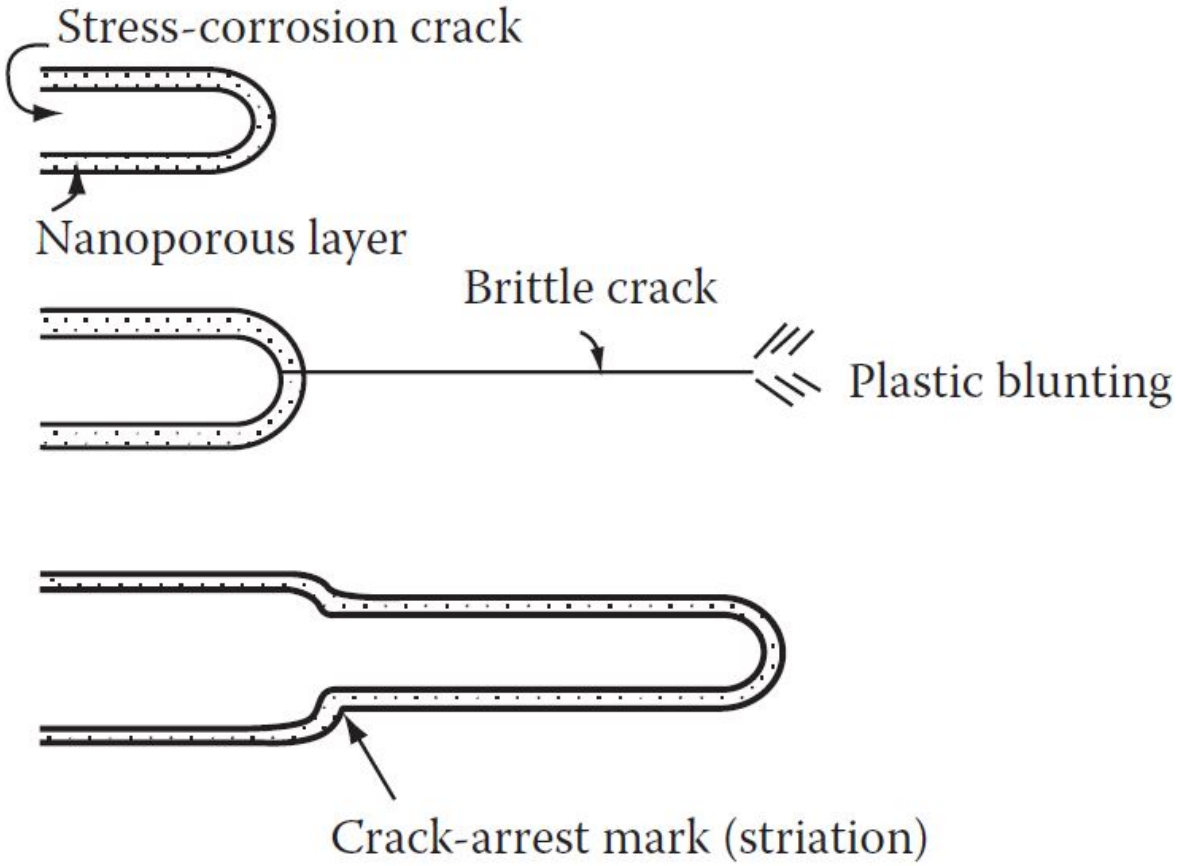

Figure 2.6. Schematic illustration of film-induced cleavage model for crack propagation

3. EXPERIMENTAL

3.1 Sample Material and Weld

Two hot rolled SS304L (UNS S30403) sheets of 3mm thickness with composition shown in Table. 3.1 were used to prepare the specimens. Following Canister Mockup report by SNL [65], 30-degree bevels were prepared on sheet edges. Gas tungsten arc welding (GTAW) was performed following parameters in Table 3.2 with SS308L (UNS S30880) filler. A schematic diagram for the welded sample is depicted in Figure 3.1. The welded sheet was sectioned using laser beam to 105mm X 18.5mm following ASTM G39 standard with welding bead in the middle and ground flat afterward [66].

3.2 Metallurgical Preparation

To prepare samples for mechanical and microscopic examination, part of interest on the sample was sectioned by diamond circular saw to minimize deformation and residual stress introduction. All of the samples were sectioned such that fusion zone, heat affected zone (HAZ), and base metal were included, as represented by green box in Figure 3.1. To obtain optimal edge retention, samples were pressed-mounted in graphite-blend conductive mounting resin with the cross section facing out. The press mount was conducted at 200 °C, 3000 PSI for 12 minutes. Mechanical polishing was done on BUEHLER EcoMet30 semi-automated polishing system with the following procedure:

1. 360 grit SiC paper, 20N force, 200 RPM, 2 mins
2. 600 grit SiC paper, 20N force, 200 RPM, 2 mins
3. 800 grit SiC paper, 20N force, 200 RPM, 2 mins
4. 1000 grit SiC paper, 20N force, 200 RPM, 1 mins
5. 1200 grit SiC paper, 20N force, 200 RPM, 1 mins

Final mirror-like polishing was done by vibratory polishing with 0.05um colloidal silica for 4 to 6 hours. To avoid residual silica, after vibratory polishing, samples were immediately

transferred into micro-organic soap solution and ultrasonic cleaned for 15 minutes. Final cleaning was done by ultrasonic cleaning with Acetone and Isopropanol, followed by air-blow drying.

3.3 Four Point Bending Test

To simulate the residual tensile stress for SCC initiation, four point bending test was conducted following ASTM G39 standard [66]. The loading fixture was made by highly corrosion resistant Hastelloy C-276 superalloy. To avoid generation of superimposed galvanic current, the contact points between the sample and the fixture are supported by teflon pillars, as shown in Figure 3.5. The sample was first loaded into the fixture and indented by the loading bolt, as shown in Figure 3.2. Longitudinal tensile stress is applied to the convex side of the sample as the loading bolt is screwed to indent the sample. To calculate stress applied, deflection of specimens was determined by separate strain gauge. Maximum tensile stress applied on the test coupon's convex side was calculated based on the equation [66]:

$$\sigma = \frac{12Ety}{(3H^2 - 4A^2)} \tag{3.1}$$

where σ is maximum tensile stress, E is modulus of elasticity, t is thickness of specimen, y is maximum deflection (between outer supports), H is distance between outer supports, A is distance between inner and outer supports

In addition, indentation force can also be converted from tensile stress by:

$$\sigma = \frac{3PL}{4bd^2} \tag{3.2}$$

where P is Indentation load, L is Outer support span, b is Width of the sample, d is thickness of the sample.

Each sample's dimension were measured, and maximum deflection was calculated by reading the strain gauge on the apparatus. Because plastic deformation involves localized dislocation motions and is hard to quantify based on macroscopic measurement, the calculation of this standard only applies to the elastically stress scenario. However, as part of the

primary goal of this research was to simulate real SCC condition of SNF canisters, based on the deep hole drilling measurements of residual stress in the mockup report [65][67], 380 MPa maximum residual tensile stress was implemented for the four point bending test.

After samples were loaded with the bending fixture, they were set in air at least few days before performing corrosion to allow depassivation.

3.4 Boiling Magnesium Chloride Corrosion Test

Boiling magnesium chloride corrosion test has been a standard test method for testing SCC susceptibility for various stainless steel for many years after its introduction in 1945 [68][69]. Boiling magnesium chloride corrosion test for this thesis was performed on prepared samples to understand stress cracking corrosion susceptibility in Advanced Materials Laboratory at University of New Mexico and the setup is shown in Figure 3.3. The cooling system ran cooled DI water through the condenser to cool the water vapor from the boiling of the $MgCl_2$ solution and maintain the stable boiling temperature continuously. The boiling solution was made by adding DI water to reagent grade magnesium chloride hexahydrate flake in the boiling flask. From the relationship between boiling points of $MgCl_2$ solutions at one atmosphere pressure and solution concentration [70], to maintain the required 155.0 $\pm$ 1.0°C (311.0 $\pm$ 1.8°F) boiling temperature, the concentration of the $MgCl_2$ solution was set to 54.3 wt%. To make the desired solution, 1200.0g magnesium chloride hexahydrate flake was measured and loaded into the boiling flask with 30.0mL DI water and 2000 glass beads as boiling aid. Two of the test coupons were placed once in the flask vertically and the system was sealed and brought to boil. To adjust the boiling temperature to desired value after the boiling was stable, 10.0mL DI water (if want to decrease boiling temperature) or 5.0g $MgCl_2$ hexahydrate flake (if want to increase boiling temperature) was added carefully through the side trap on top of the boiling flask. Temperature of the boiling solution was monitored and recorded via the thermometer inserted into the solution every half hour to make sure temperature is stable and within the desired range.

After every 6 to 8 hours of boiling, specimens were taken out and cleaned to check for crack initiation. The outer surface that was under tensile stress was examined under optical microscope at 20X-50x, as specified in ASTM G36 standard [68]. After micro cracks were

found on sample surface, samples were ultra-sonicated in DI water followed by nitric acid to remove corrosion product.

3.5 Electron Microscopy Characterization

The Scanning Electron Microscope (SEM) is one of the most commonly used characterization instruments in both academic and industry, because of its high resolution and magnification, wide range of imaging capability, and large depth of focus [71]. SEM uses a focused high-energy electron beam to scan sample surface and collects the signals produced from the interaction between electron and matter to obtain high-resolution images. As the electron beam interacts with the sample, it will go through elastic and inelastic scatterings, emitting various signals, as shown in Figure 3.4 [71][72]. Even though there are many different types of signals generated, not all of them will be detected and used. Most of the commonly used signals are secondary electron (SE) and backscattered electron (BSE). SE is a type of low energy electrons produced from ionization of specimen atoms caused by incident electrons. It can reveal the topology of the sample with good signal to noise ratio. BSE results from the elastic scattering of of the primary electrons. Typical scattering angle ranges from 0 - 180 degrees. Because the yield of backscattered electrons is proportional to atomic number, BSE is often used to reveal elemental distribution [71]. In addition, scattering angle and yield of BSE are also sensitive to crystal structure, which leads to the introduction of electron backscatter diffraction (EBSD) for crystallographic characterization.

Since its automation [73], EBSD has become an major technique to analyze texture and anisotropic properties of polycrysatlline materials. A mirror-polished sample needs to be tilted to a high angle (70° in this thesis) in the SEM. Upon interaction with the specimen, electrons experience initial elastic scattering and two cones of diffracted electrons for each crystal lattice are produced when Bragg condition is satisfied [74][75]. A phosphor screen is placed horizontally close to the sample to capture a wide angle of the diffracted electron. When the diffracted cones enter the phosphor screen, "Kikuchi band" forms and corresponds to specific family of crystal lattice planes. These Kikuchi bands will be calculated and compared with theoretical data of different phases and crystallographic orientations by EBSD software (EDAX OIM V8 in this thesis) automatically. In recent decades, 3D EBSD

was developed by consecutive slicing and EBSD scanning to reveal 3D topography of crystal lattices [76][77][78].

In this research work, SE and EBSD are mostly used for topographic and crystallographic analysis. An FEI (now Thermo Fisher Scientific) Quanta 650 FEG SEM was used for EBSD scanning. The voltage of the SEM was set at 20kV, and the current was 5nA for the electron beam. Dwelling time and step size are set to be 1ms and 0.3-2.5 um/pixel. Neighboring confidence index (CI) was set to be above 0.1, and neighboring grain tolerance angle was 3°. EDAX OIM 8 was used for data analysis. In this thesis, all electron microscopy characterization and analysis were performed on the cross section of the sample in Figure 3.1, as sample surface defined as the convex sample side in the bending fixture.

3.6 Finite Element Analysis

To gain better understanding of the stress distribution over the test coupon, finite element analysis was performed on standard dimension coupon models. FEA simulation was done in ABAQUS by 3DS Academy. Because the weld was single pass, heat-affected zone (HAZ) was assumed to be symmetrical over the welding bead [79]. Mechanical properties listed in Table 1 were used in the modeling. Four rigid bars were modeled rigid and the middle two bars indented to apply desired residual stress to the specimen, as shown in Figure 3. The outside surface of the middle, which is the welding bead, on the specimen experienced the highest tensile stress, as expected from the real canister wall case. The FEA model informed us the calculated indentation displacement needed for reaching desired 400 MPa residual tensile stress in our real 4-point bending fixture loading.

3.7 X-ray Diffraction Crystallography (XRD)

X-ray Diffraction Crystallography

According to ASTM G-36 [68], residual stress calculated from equation 3.1 is only valid in elastic region. To verify the amount of residual stress introduced by four-point bending test, XRD measurement was done on the sample surface in lateral direction starting from the

center weld zone. Pulstec u-360 XRD was used for the residual stress measurement because of sample size constraint.

In this thesis, all of the XRD residual stress measurement was performed on the sample convex surface as in the bending fixture.

Table 3.1. Chemical composition ad mechanical property of the austenitic stainless steels used in this study (UNS S30403 and UNS S30880)

Material	Alloying wt.% balance Fe										Yield Strength	Tensile Strength	Elongation
	C	Si	Cr	P	S	N	Mn	Ni	Mo	Cu	(MPa)	(MPa)	%
S30403	0.027	0.35	18.11	0.023	0.004	0.056	1.31	8.02	–	–	273	699	64
S30880	0.014	0.47	19.88	0.021	0.002	–	1.83	9.66	0.01	0.10	–	580	29

Table 3.2. TIG welding parameters

	Interpass temperature (°F)	Current (A)	Voltage (V)
Pass 1	75	110	12
Pass 2	266	110	12

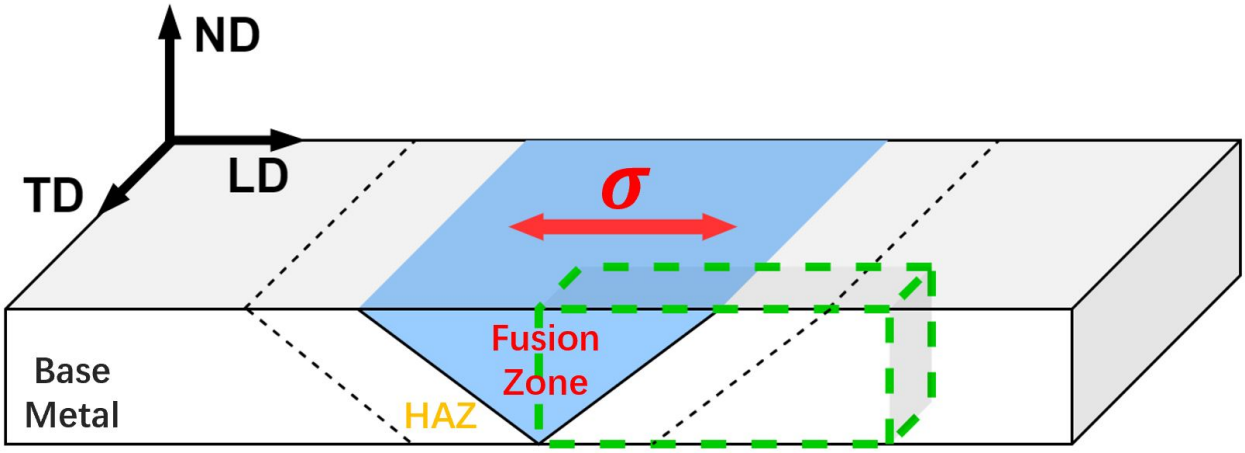

Figure 3.1. Schematic diagram of GTAW welded sample

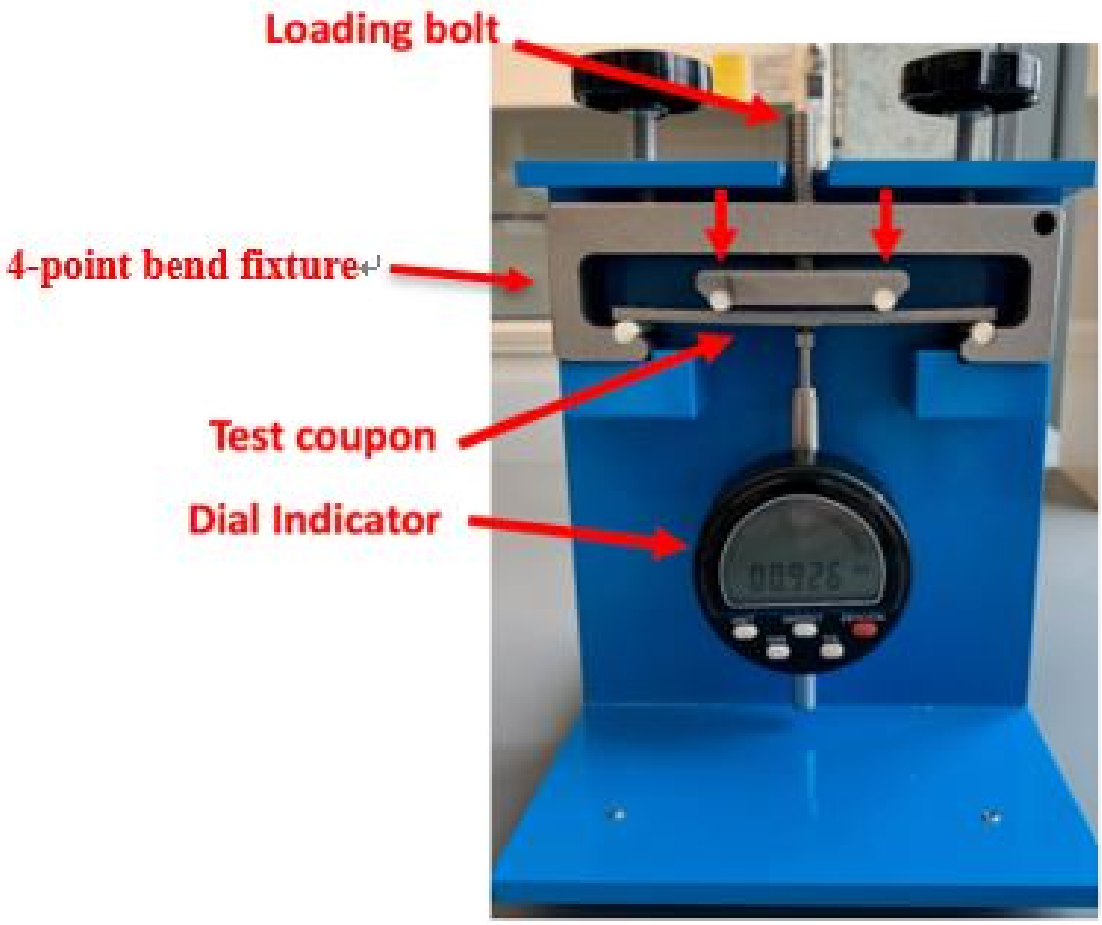

Figure 3.2. 4-point bending test setup

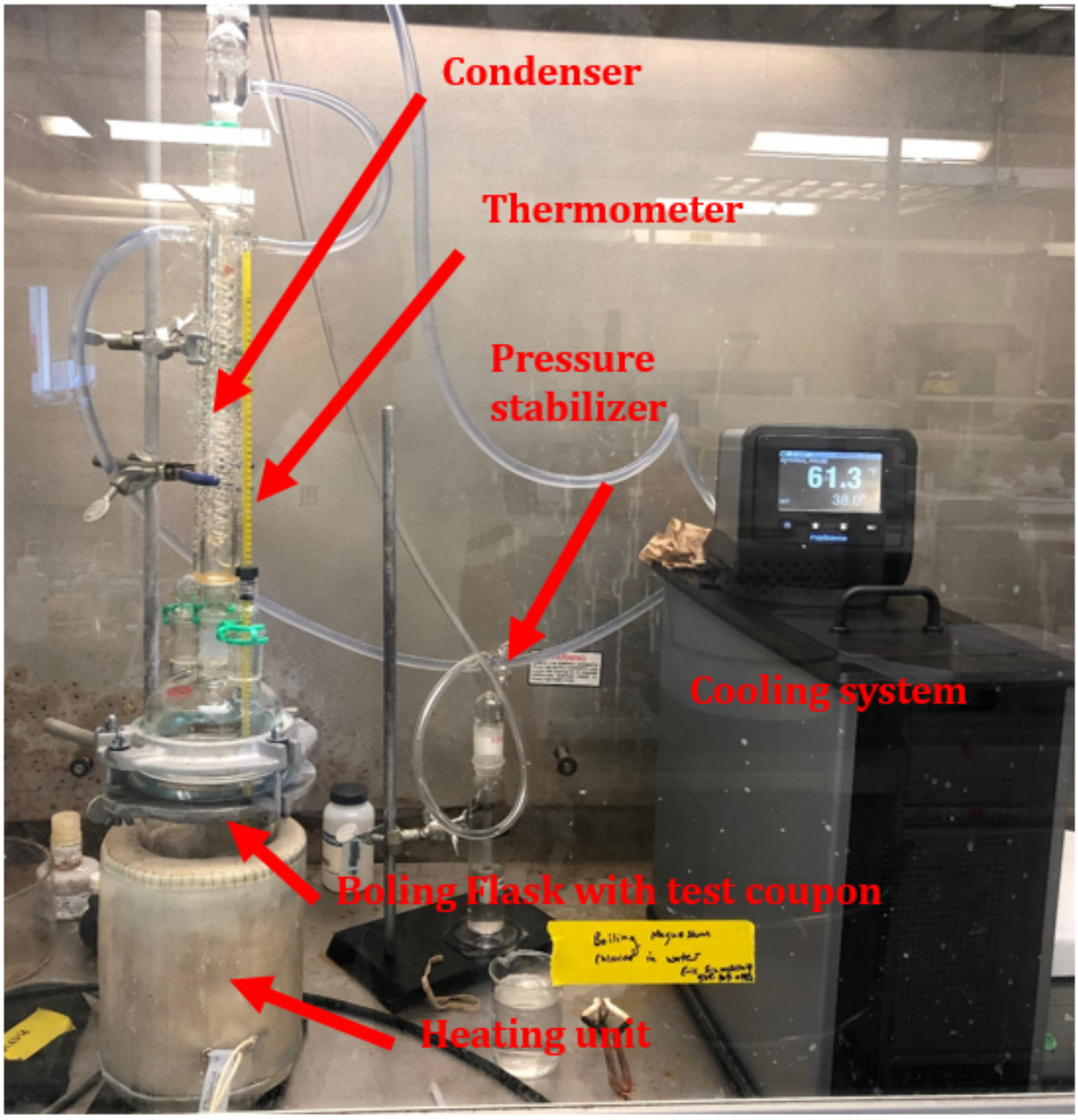

Figure 3.3. Apparatus for boiling magnesium chloride corrosion test at UNM

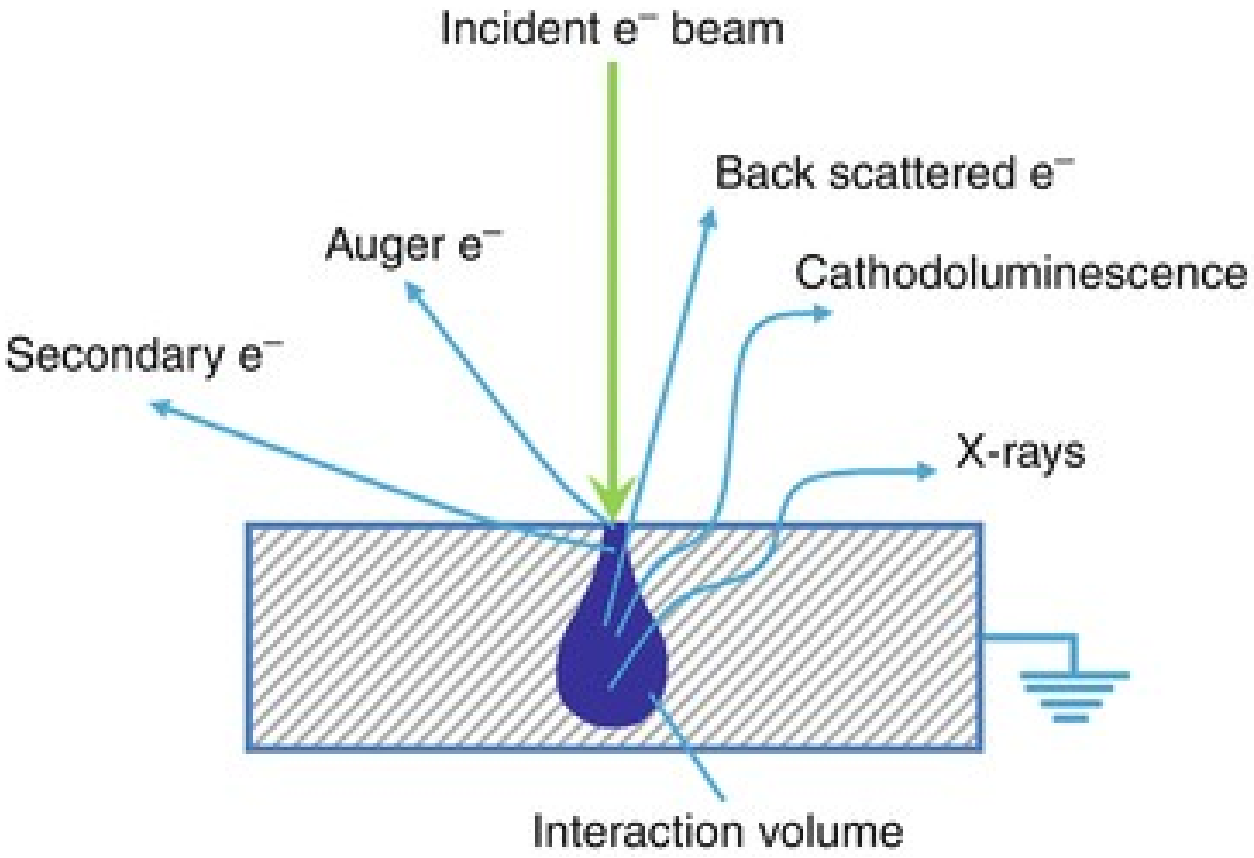

Figure 3.4. Signals generated by interaction between electron beam and sample [71]

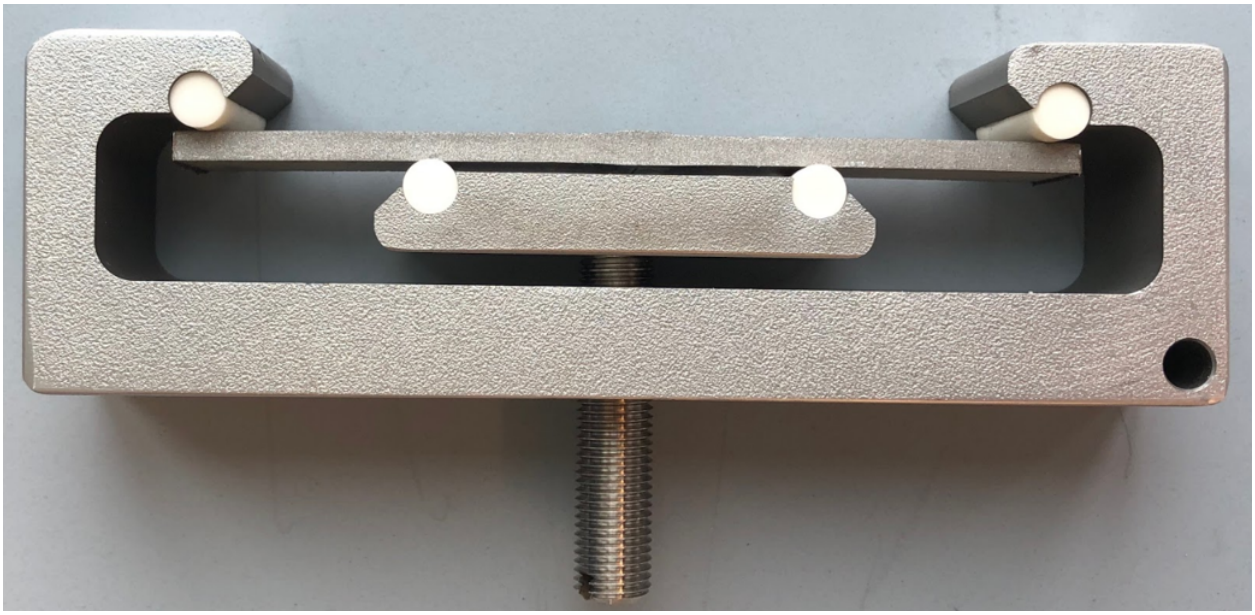

Figure 3.5. Four-point bent sample in the bending fixture

4. RESULTS

4.1 X-Ray Residual Stress Measurement

XRD residual stress measurement is performed in the lateral direction on the as-received and four-point bent sample surface. As shown in Fig 4.1, As-received sample shows only moderate compressive residual stress in the HAZ and base metal. From the calculation of equation 3.1, maximum tensile stress (380 MPa) is applied at the center of the weld zone. However, in the weld zone of 380 MPa stressed sample, large (around -400 MPa) compressive residual stress is detected. This is attributed to inaccurate measurement caused by the irregular shape of the weld bead. The accuracy of XRD measurement is closely related with surface flatness [80]. On the contrary, the rest section of the sample is flat, and XRD measurement showed decreasing tensile stress from sample center towards end. External stress applied by four-point bending is calculated as the difference between the residual stress of the as-received and the four-point bent sample, as shown in Figure 4.2.

4.2 FEA Simulation

An illustration of the final FEA simulation for four-point bent sample is shown in Figure 4.3. Most of the tensile stress concentrates near the center of the convex side of the sample. Specifically, the area with the highest tensile stress (red level) is between the two supporting beams, as shown in Figure 3.5. Simulated residual stress is also plotted in Figure 4.2 to compare with the actual stress applied from XRD measurement. It is observed that simulated stress is the same between supporting pillars (+/- 22.5 mm). In HAZ zone, XRD measurement is consistently around 100 MPa lower than simulated result. As the current FEA simulation only simulate elastic deformation behavior, this difference indicates plastic deformation happens during bending. In weld zone, because of the inaccurate XRD stress measurement, the calculated external stress is also not representative. However, since the XRD measurement in HAZ, which is the major part of the studied area, is consistently lower than simulation, it is reasonable to assume external load applied in the weld zone is also lower than the simulation. There are two purposes for FEA simulation: 1. FEA model is used to confirm the amount of residual stress applied by bending fixture and verify the pres-

ence of plastic deformation during the loading. 2. FEA result indicates convex surface of the sample share the same maximum principal tensile stress between the middle two supporting bars. (This helps to unify the stress intensity calculation in fracture mechanics)

4.3 Crack Statistical Analysis

After corrosion, crack location and frequency are recorded by examining cross section of the sample under SEM. The number of cracks in weld zone and HAZ is normalized by the length of the area because they share the same width, as shown in Figure 4.4. A total of 138 cracks are found near the center of the sample, with 31 cracks in weld zone and 107 cracks in HAZ. 35 cracks of interest morphology are picked for further crystallographic analysis with EBSD. Most of the cracks are less than 10 um (microcrack). From EBSD analysis, these microcracks just showed crack initiation with limited propagation within the initiation grain. Both of the weld and HAZ had macrocracks (larger than 20 um) that propagated perpendicular to the tensile stress direction. However, the chance for microcracks to propagate and grow further is limited because of insufficient local stress and strain [6][81]. From the crack density, it is observed that weld zone is less susceptible than HAZ. Further characterization and analysis in the following sections are heavily focused on HAZ, because of limited access to the EBSD images on weld zone.

From the EBSD analysis, among all scanned cracks, only 8% of the crack initiation is intergranular (IGSCC), and 92% of the initiation is transgranular (TGSCC), whereas crack propagation is all TGSCC for both weld and HAZ. Limited IGSCC existence is attributed to the low carbon content in the UNS SS304L substrate. Ultra-low carbon content in the material limit sensitization during cooling and carbon segregation on grain boundaries [82]. IGSCC is thus suppressed because of insusceptible GB in the current corroded sample.

4.4 SEM Characterization Results

Crack morphology: as shown in Figure 4.5, cracks show typical cleavage appearance that clearly cross grain boundaries and pass through grains, indicating the brittle nature of the TGSCC. Overall, cracks are perpendicular to the tensile stress direction, as applied

by the bending fixture. Most of the microcracks exhibit limited branching; on the contrary, developed macrocracks show moderate branching intersection, like crack C60 in Figure 4.16. Developed cracks propagate in a zig-zag pattern in twins. As EBSD results later show that crack orientation changes every time cracks enter and exit grain twins, as marked on the bottom in Figure 4.15 and Figure 4.16. Because slip systems in twins are mirrored as the original grain, crack orientation deviation in every twin is a direct evidence that crack propagates along slip planes, which is {111} for FCC crystals. Cross-section view of river pattern marks are also observed as discontinuous coalescence in certain grains, as marked on the top in Figure 4.15 and Figure 4.16.

4.5 EBSD Characterization Results

From the EBSD images, the average grain size for HAZ and weld zone are 56.3 um and 431 um respectively. Because of edge round off and charging of mounting epoxy, the very edge of the corroded sample could not be indexed by EBSD detector. The information of the beginning portion (5-10 um) of crack initiation is thus not accessible, as indicated by the constant black or noisy zones on the bottom of the EBSD images. Most cracks are TGSCC, clearly passing through GBs. To help visualize the crack pattern, sketchy crack paths are drawn over the EBSD map. To better aid the observation of crack details, SEM images of corresponding crack are resized and arranged, such that it matched exactly with adjacent EBSD map. Red arrows indicate the crack propagation direction and tensile stress direction is marked on the top. Example EBSD maps for cracks with special crack propagation phenomena are listed at the end of this chapter 4.14, 4.15, 4.16, 4.17.

As shown in Figure 4.12, both dendritic austenitic structure and δ ferrite interdendritic structure are observed. During the cooling process after the weld, primary δ ferrite developed from solidification at high temperature, and then transformed to γ austenite as temperature decreases [67]. However, because of the rapid cooling rate, diffusion controlled δ-γ transformation couldn't complete and σ ferrite retained within grains and near grain boundaries [83][84][67].

As shown in Figure 4.14 4.15 4.16 4.17, twinning distributes homogeneously in different grains across the whole HAZ. coincident site lattice boundaries (CSL) are marked as black

grain boundaries in the EBSD maps. Since Austenitic stainless steel has a moderate SFE between 100K to 300K [53][54], plastic deformation is accommodated mainly by slip and twinning.

4.5.1 Grain Orientation Analysis

Grain orientation of individual grains on sample surface and crack path are extracted from EDAX OIM software and mapped in inverse pole figure (IPF) via MTEX [78] in Matlab. All of the orientations are observed with pole normal to the cross section side of the sample. For reference, Schmid factor and Taylor factor distribution on IPF map by Hosford are also included, as shown in Figure 4.7a 4.7b [59].

Figure 4.6a shows the grain orientation distribution of grains on the sample surface that are free from cracks initiation. It is observed that the sample surface is randomly oriented with no orientation concentration.

Figure 4.6b shows the grain orientation distribution of grains on the sample surface that exhibit SCC initiation. It is observed that {011} orientation is not favored for TGSCC initiation, whereas {111} and {011} are moderately preferred for in-grain crack initiation. When combined with Figure 4.7b, it is found that most TGSCC initiation grains have middle (> 2.9) and high (> 3.3) Taylor factor.

Arrows are used to connect the grain pairs on sample surface with IGSCC initiation. Because of the function availability in MTEX, an arrow had to be used. However, the direction of the arrow didn't indicate the preferred grain orientation, since IGSCC is characterized by grain boundary condition. It is shown that most grain pairs laid along the $\{001\} - \{111\}$ direction, with no {011} grains involved. Due to the fact that IGSCC is minority in the current corrosion result (8% of total cracks), the fundamental focus of discussion and investigation would be oriented towards TGSCC.

Figure 4.6c shows the grain orientation distribution of grains on the crack path. Arrows are used to connect TGSCC grain pairs and show the propagation direction. It is observed that most transgranular crack propagation lies along the $\{001\} \leftrightarrow \{111\}$ direction. When combined with Figure 4.6b, it is observed that grain pairs along the $\{001\} \leftrightarrow \{111\}$ direction have different values for both Schmid and Taylor factors.

4.5.2 Schmid Factor and Taylor Factor

Schmid factor and Taylor factor distribution of grains on sample surface and crack path are individually calculated by EDAX OIM software and recorded in Figure 4.9a, 4.9b, 4.10a, and 4.10b. The frequency is normalized to the length of the corresponding weld and HAZ.

From Figure 4.9b, most of the grains on sample surface have high Schmid factor (> 0.42). As compared with Figure 4.9a, since the Schmid factor distribution of initiation grains share similar negative skewness, it is summarized that no preference of crack initiation is found with Schmid factor alone. On the other hand, Figure 4.10b shows a slightly negative skewed distribution of Taylor factor among all surface grains. According to Figure 4.10a, crack initiation didn't show direct preference for Taylor factor value alone, too.

4.5.3 Schmid Factor and Taylor Factor Mismatch

Since most of the cracks are TGSCC, to understand the effect of local strain and stress difference on crack propagation, difference between Schmid factor (m) and Taylor factor (M) of all grain pairs along the crack path are recorded in Figure 4.8. The mismatch values is calculated by subtracting m and M of the previous grain from the following grain in a cracked grain pair. In FCC structure, Schmid factor and Taylor factor are empirically inverse to each other, and exactly reciprocal to each other on {001} and {111} orientations [59]. Grains with low m and high M behave as "hard" grains because they are generally more resistant to plastic deformation and exhibit more strain hardening [59][85]. On the contrary, "soft" grains are characterized by high m and low M. For example, for all cases in the second quadrant, crack propagates from a high m, low M grain (soft) to a low m and high M grain (hard).

SCC propagation grain pairs concentrate in the second and forth quadrants, indicating grains with opposite Schmid factor and Taylor factor difference are more susceptible to SCC propagation. Branch intersection describes the case that crack branching intersects with current viewing plane, resulting in discontinuous appearance, as shown in Figure 4.16. Crack detour is categorized as when a crack "detours" in adjacent grains other than grains on its original path, as marked in Figure 4.17. It only happens when the crack is confronted

by a grain with higher Taylor factor (indicating larger local shear stress in the following grain), regardless of Schmid factor. Crack jump describes the case when a crack jumps over another grain on its path, as marked in Figure 4.14. Only one case of crack jump is detected. On Figure 4.8, it shows crack jump happens between two grains with large (> 1.0) Taylor factor difference, but the Schmid factor of the grains are similar. Lastly, crack mostly stops at GB before a harder grain (lower m and higher M).

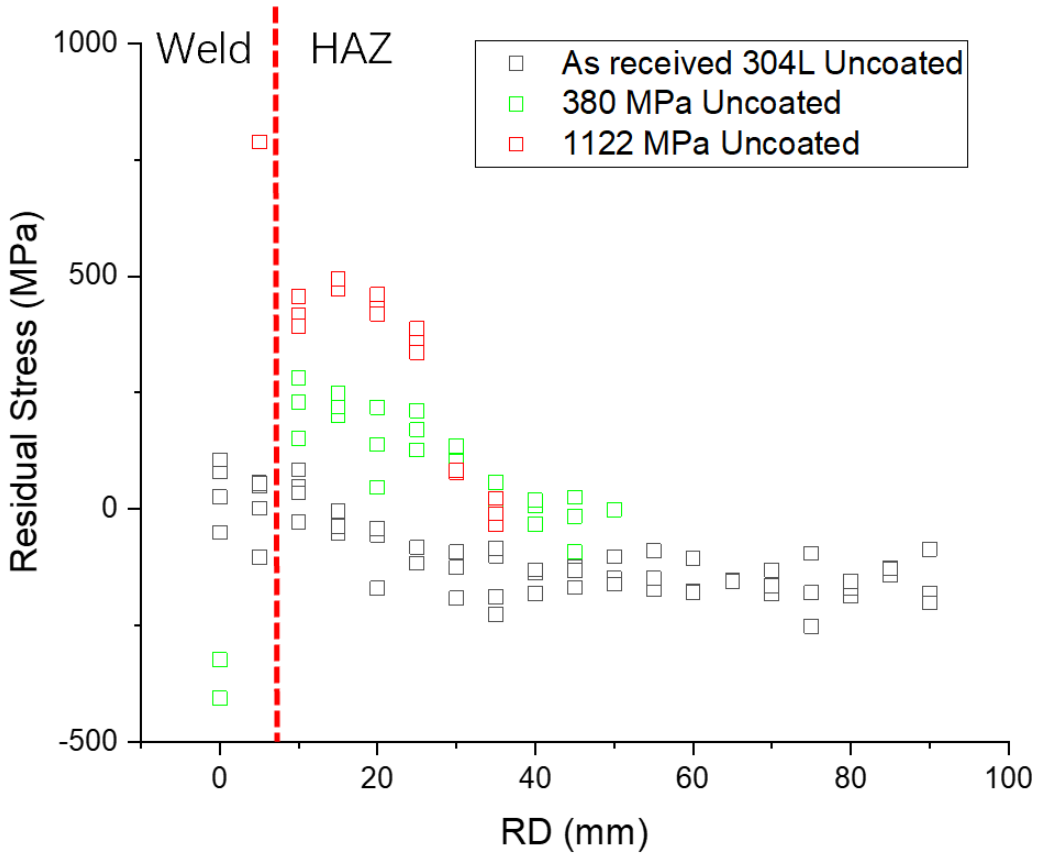

Figure 4.1. XRD residual stress measurement

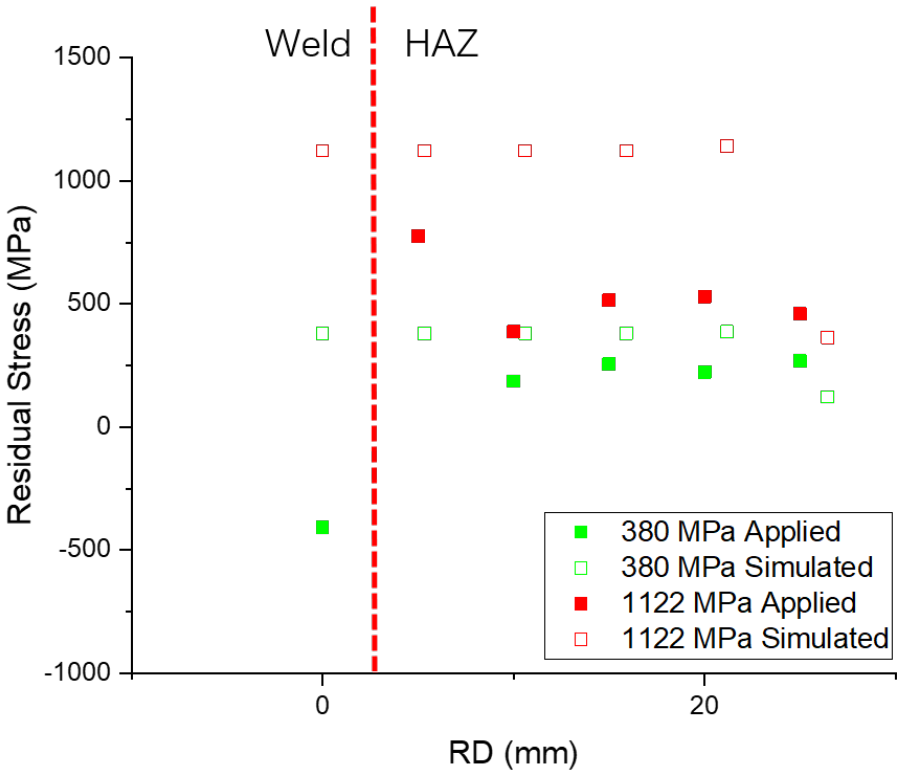

Figure 4.2. FEA simulation and XRD measurement of external stress applied by four-point bending fixture

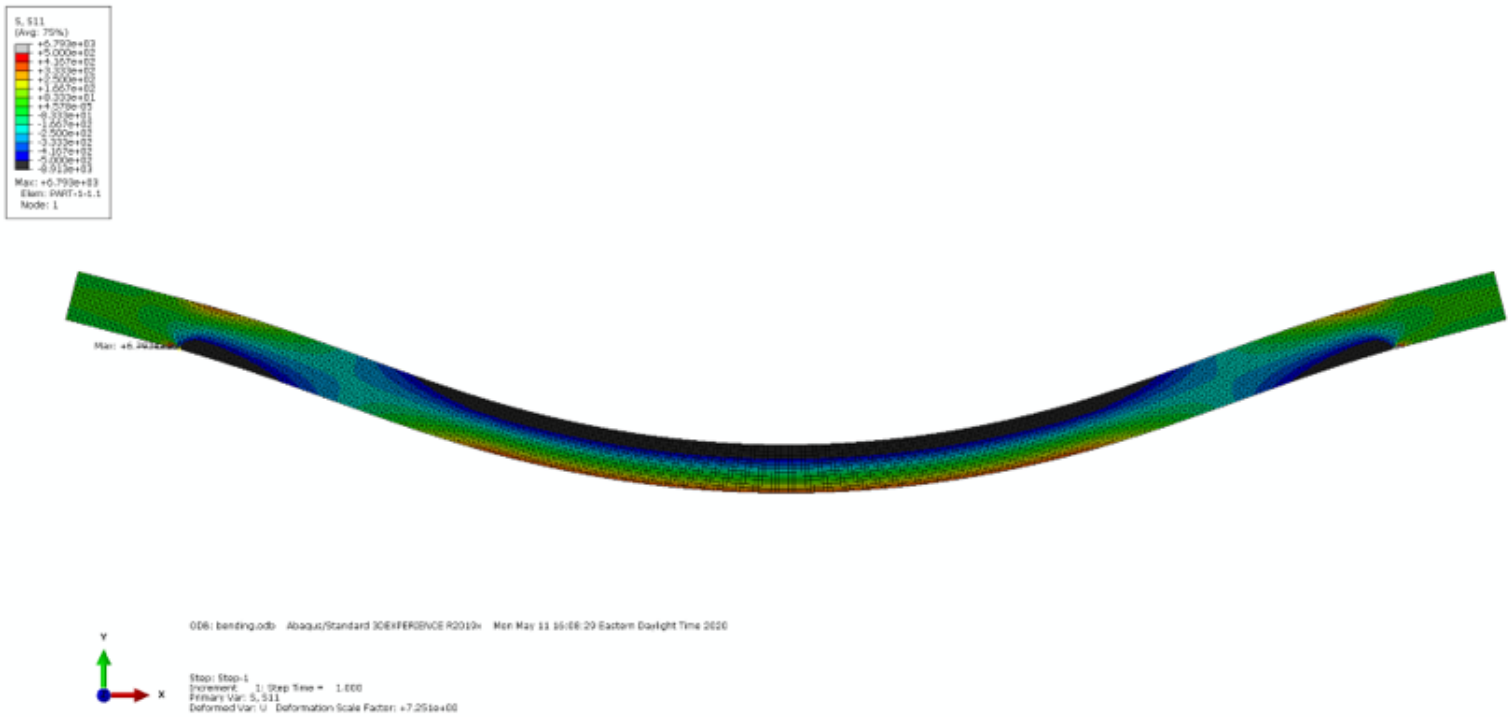

Figure 4.3. Illustration of FEA modeling for residual stress in four-point bent sample

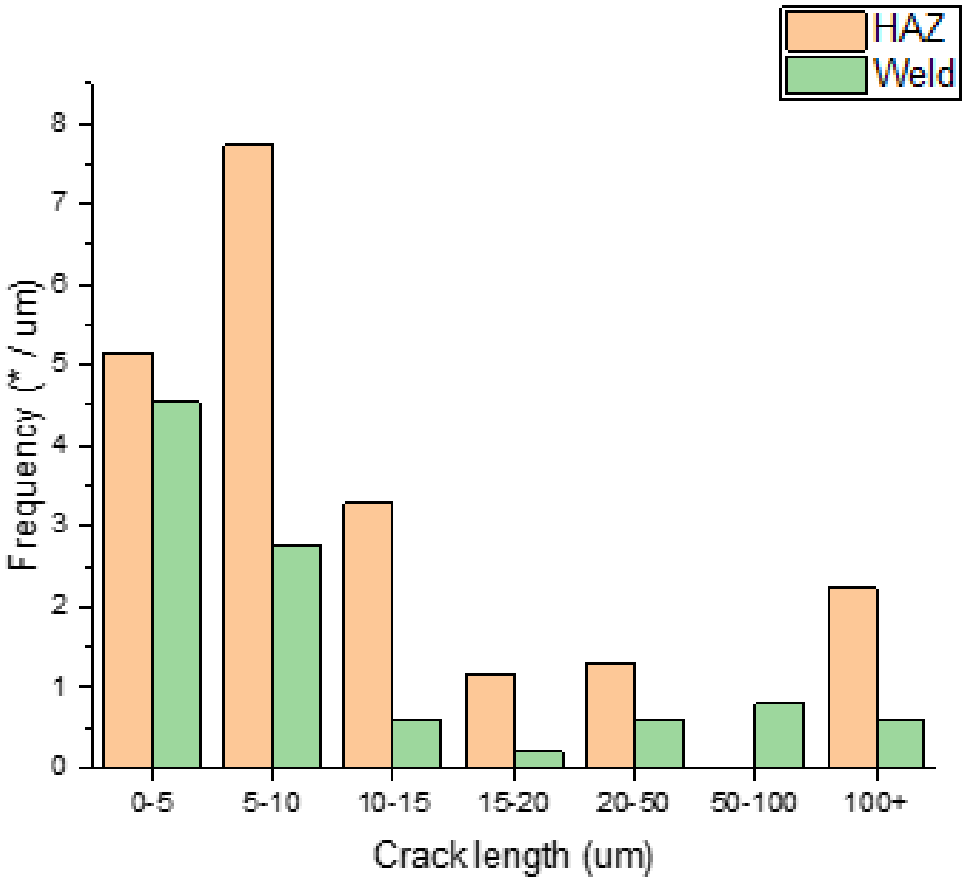

Figure 4.4. Crack density distribution of corroded sample

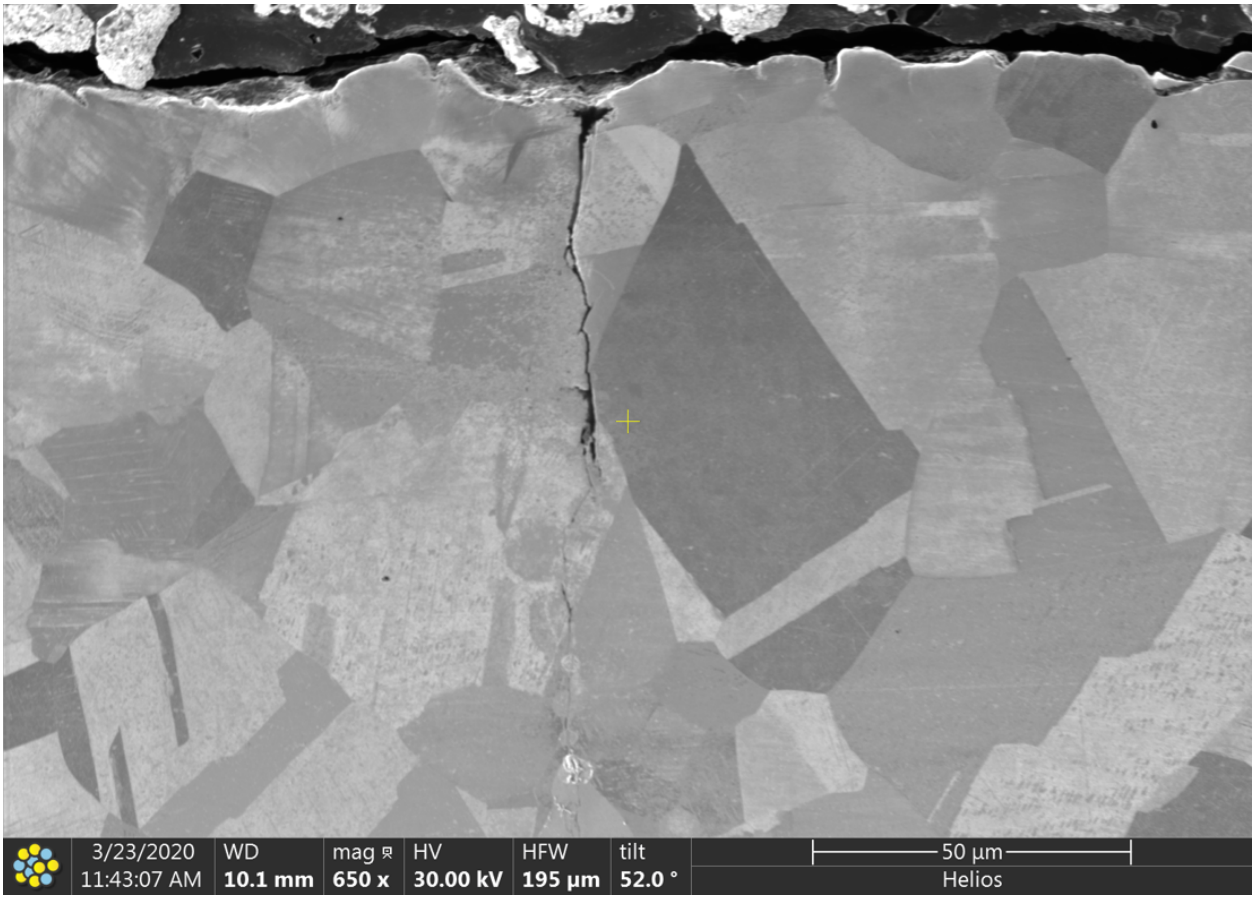

Figure 4.5. Crack Morphology Reveal after FIB polishing

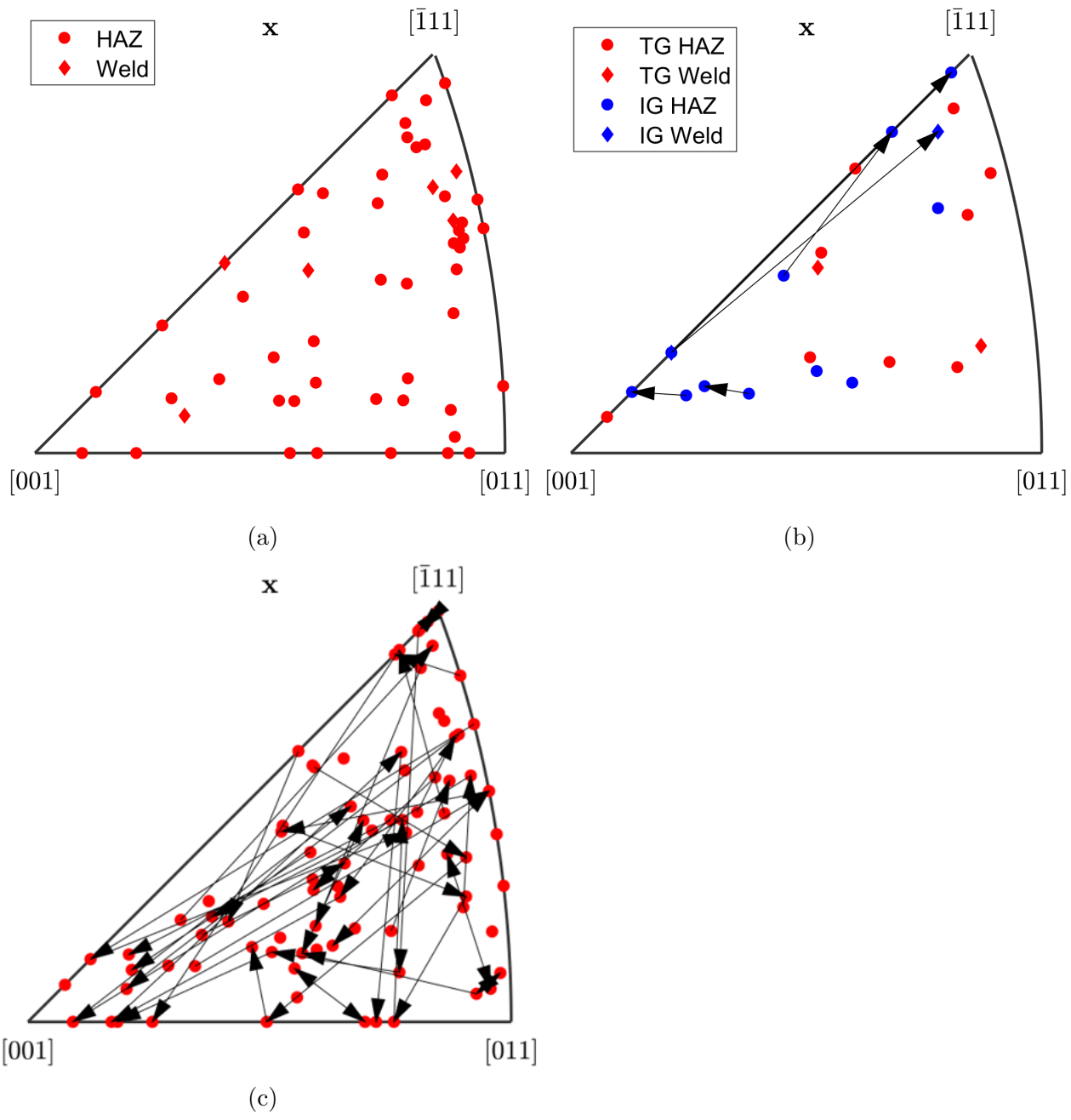

Figure 4.6. IPF grain orientation distribution for (a)surface uncracked grains; (b) surface SCC initiation grains; (c) TGSCC propagation grain pairs

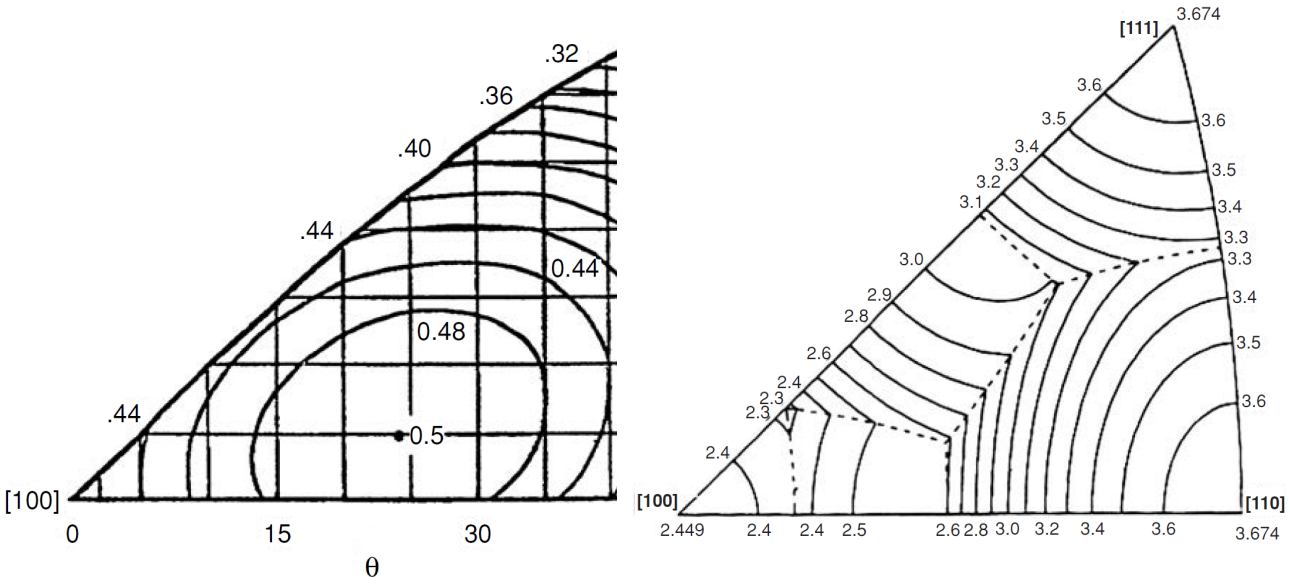

(a) (b)

Figure 4.7. (a)Schmid factor; (b) Taylor factor distribution on IPF map of FCC structure [59][86]

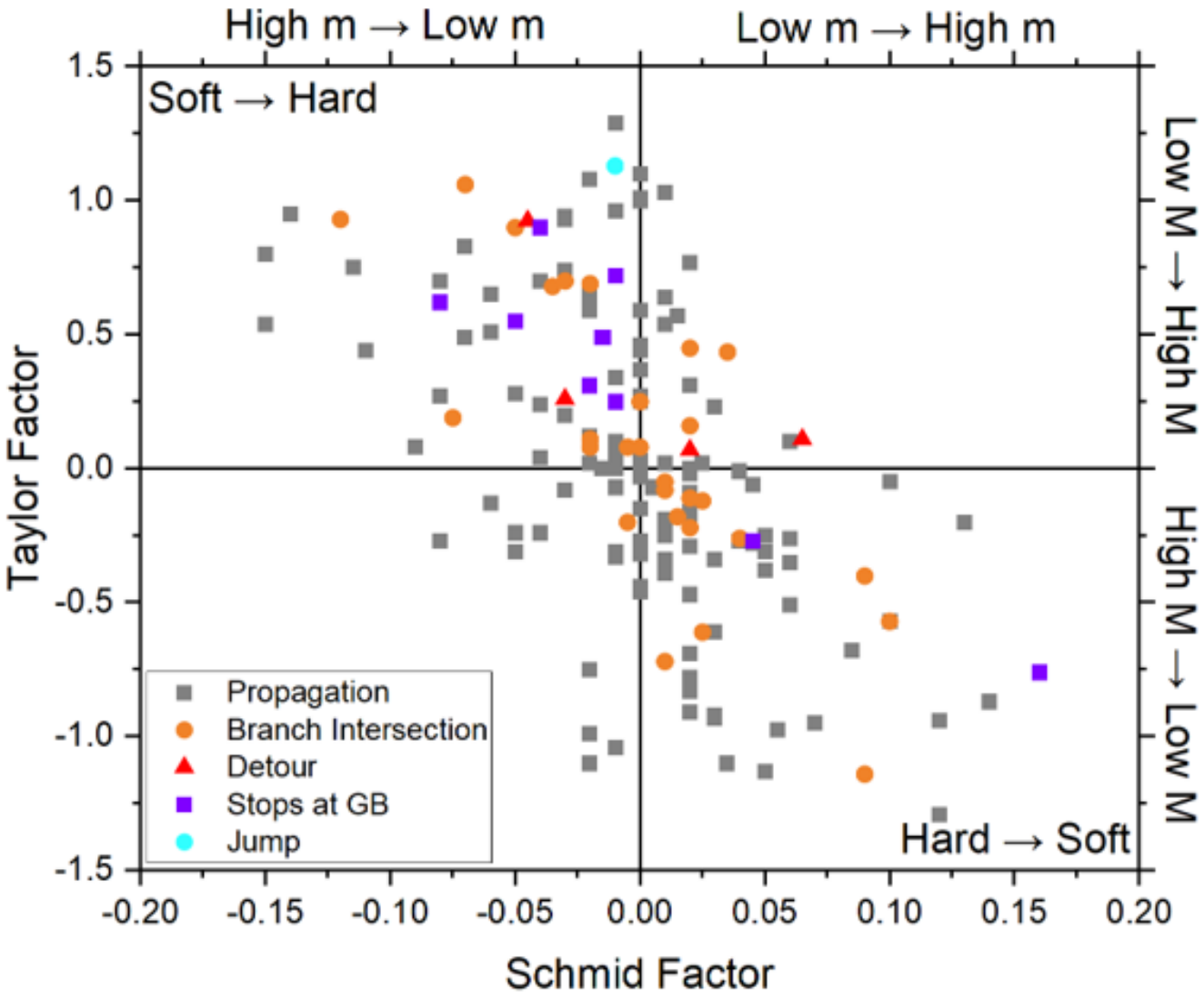

Figure 4.8. Schmid factor and Taylor factor mismatch between adjacent grains on crack path

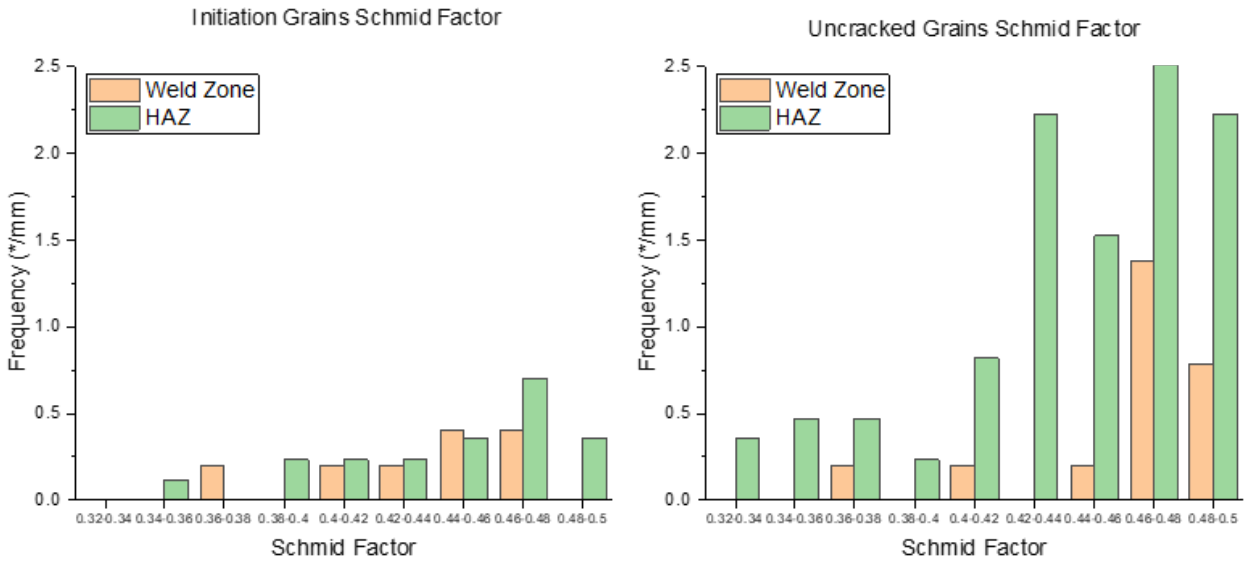

(a) (b)

Figure 4.9. Schmid factor distribution for (a)surface initiation grains; (b) surface uncracked grain

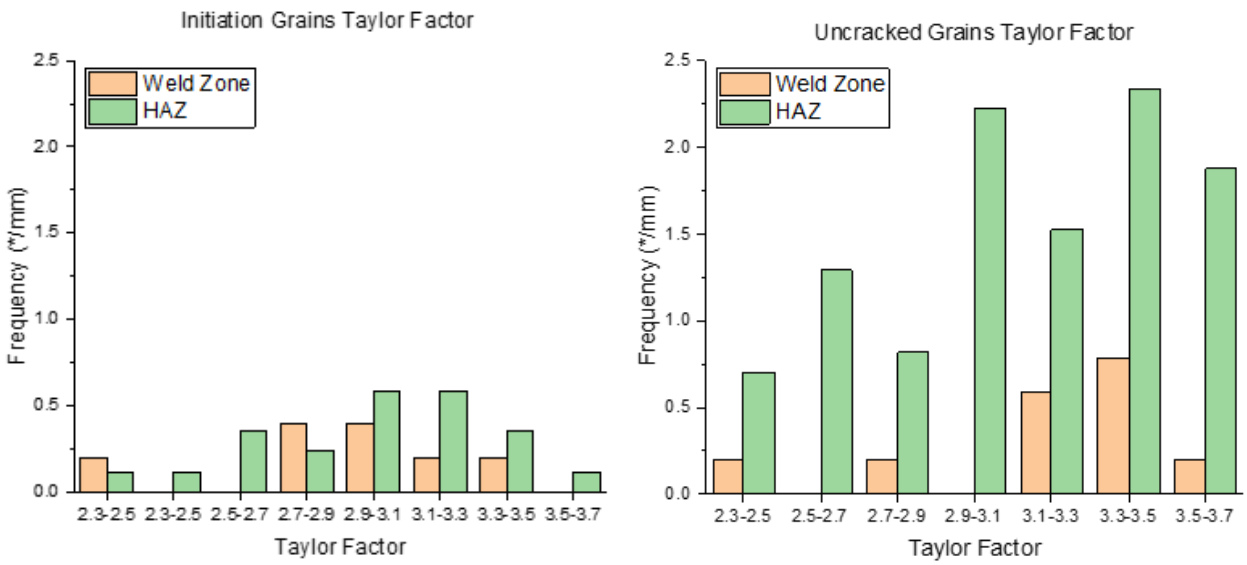

(a) (b)

Figure 4.10. Taylor factor distribution for (a)surface initiation grains; (b) surface uncracked grain

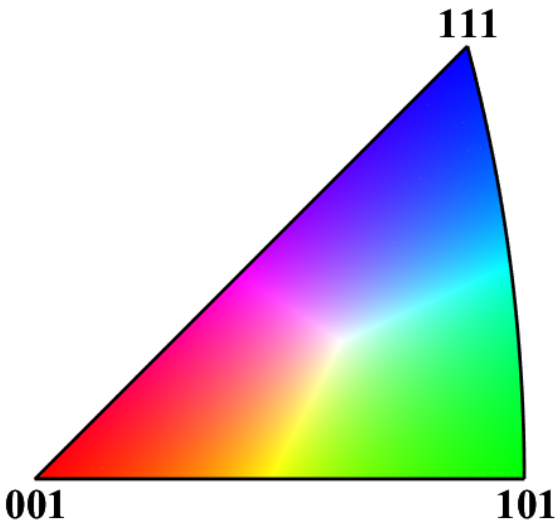

Figure 4.11. Orientation legend for IPF figures in EBSD

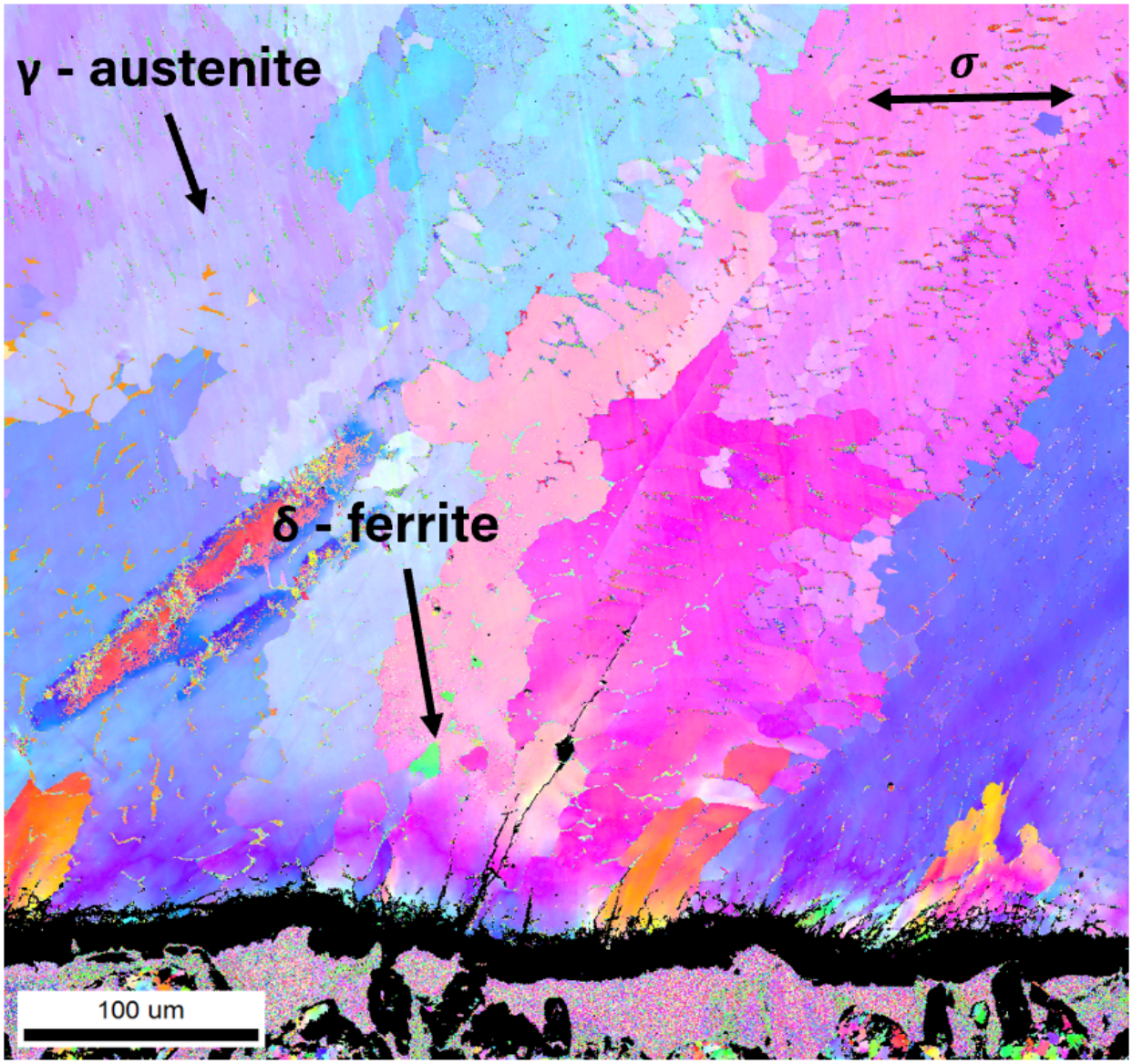

Figure 4.12. EBSD image of weld zone

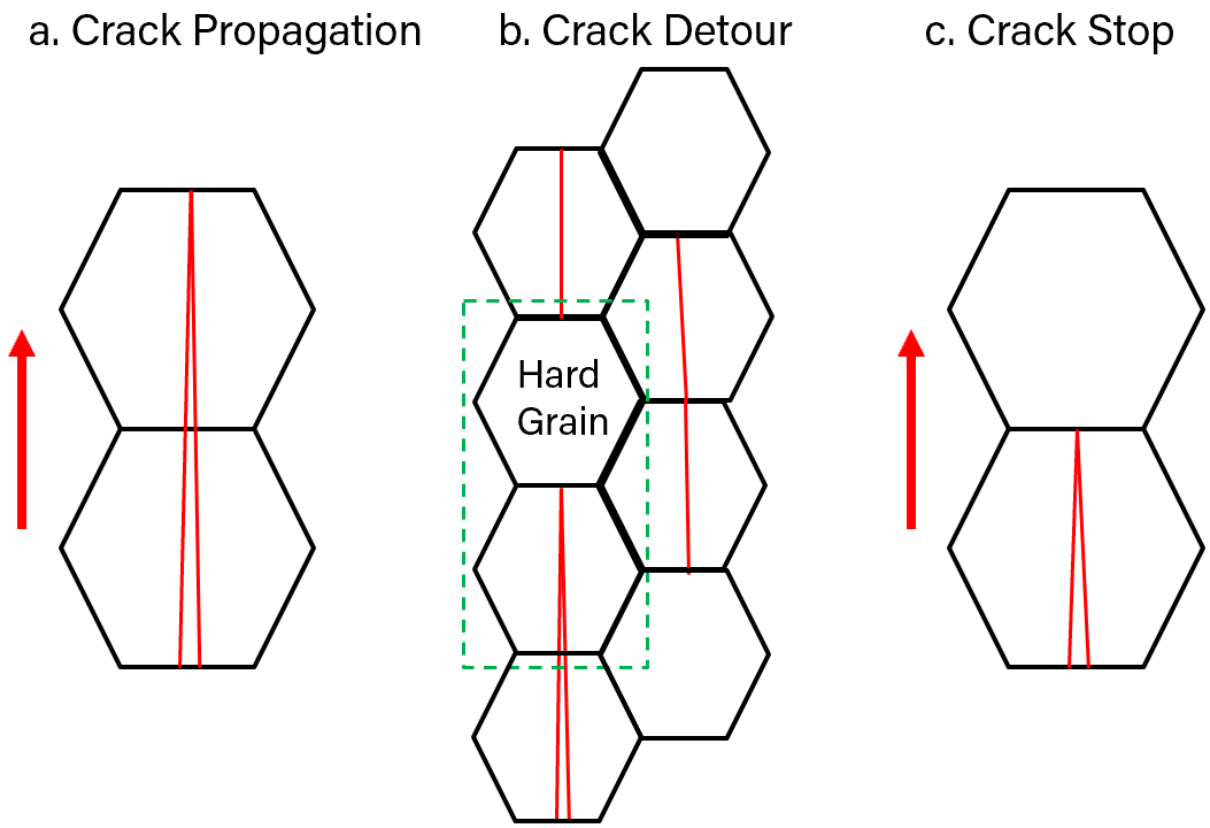

Figure 4.13. Crack Propagation Behavior Demonstration: a. Crack Propagation; b. Crack Detour; c. Crack Stop

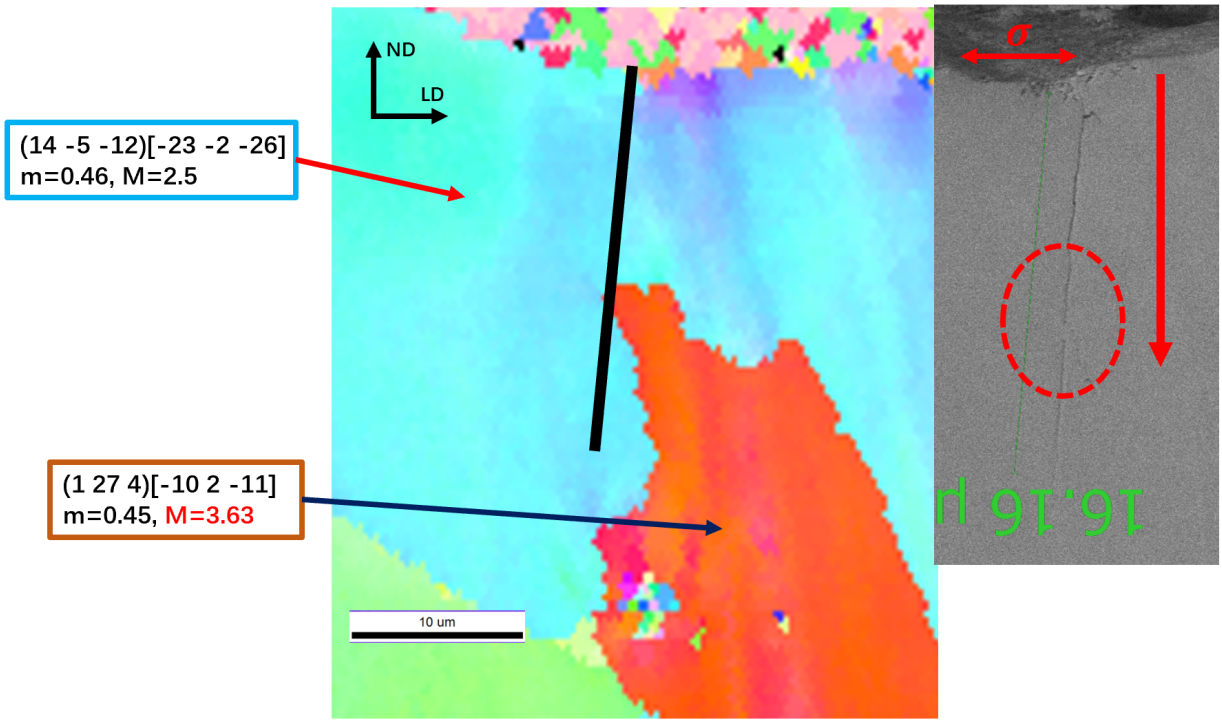

Figure 4.14. EBSD and SEM map of C48 crack with grain orientation, Schmid factor, and Taylor factor labeled. Notice the crack jump circled on the SEM image

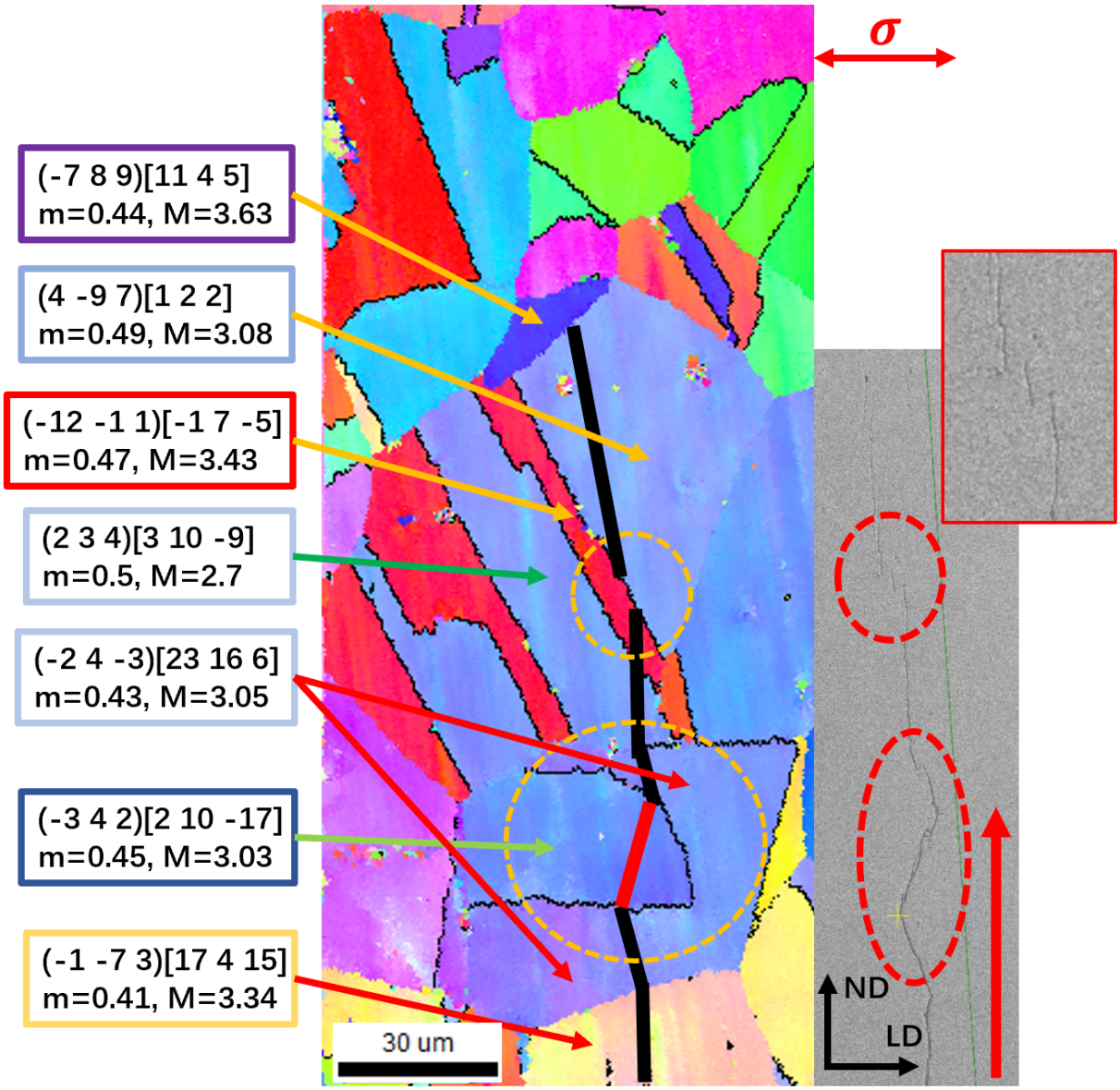

Figure 4.15. EBSD and SEM map of C54 crack with grain orientation, Schmid factor, and Taylor factor labeled. Notice the crack plane deflection circled on the bottom and Branch intersection on the top

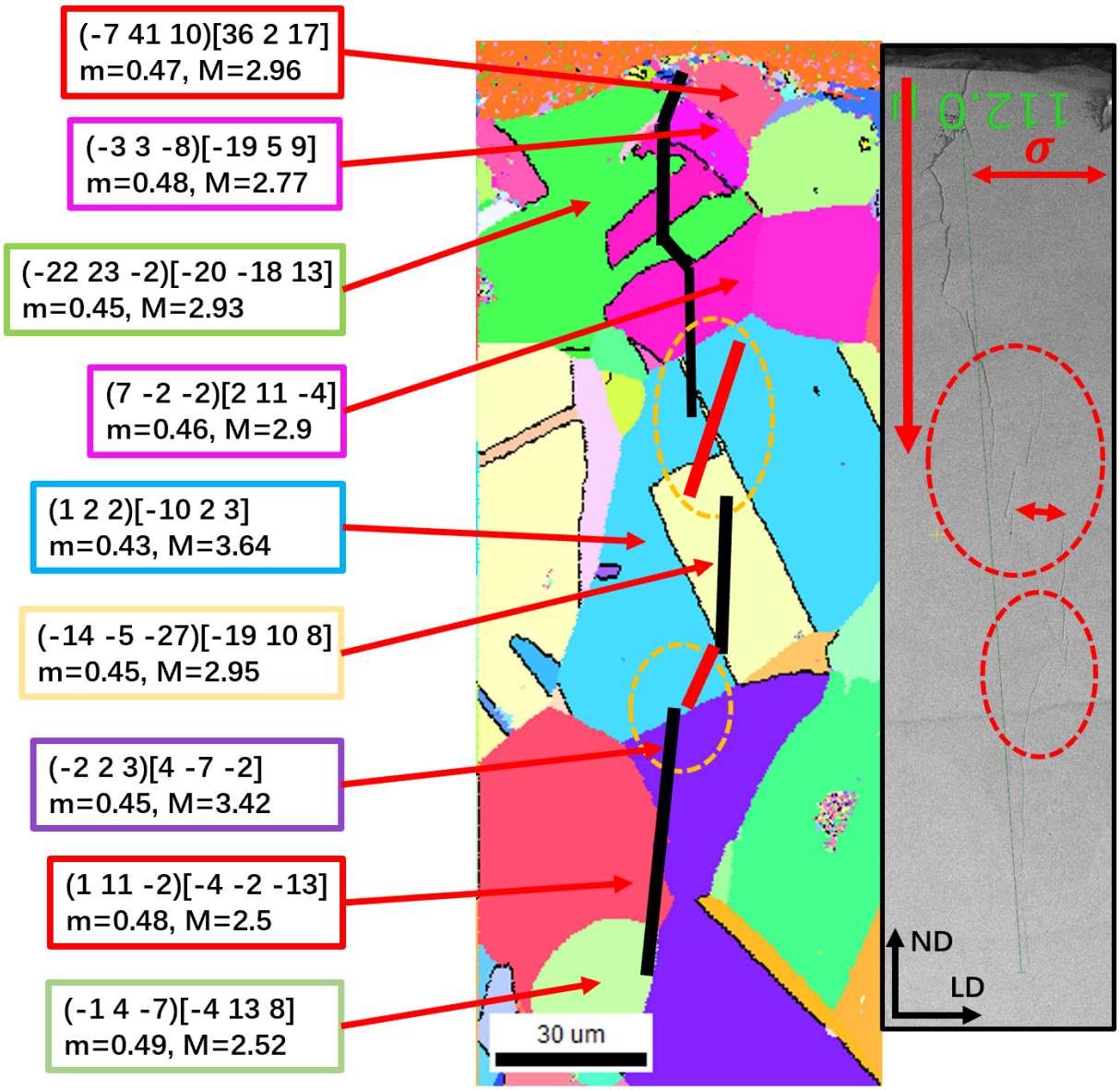

Figure 4.16. EBSD and SEM map of C60 crack with grain orientation, Schmid factor, and Taylor factor labeled. Notice the crack jump circled on the right

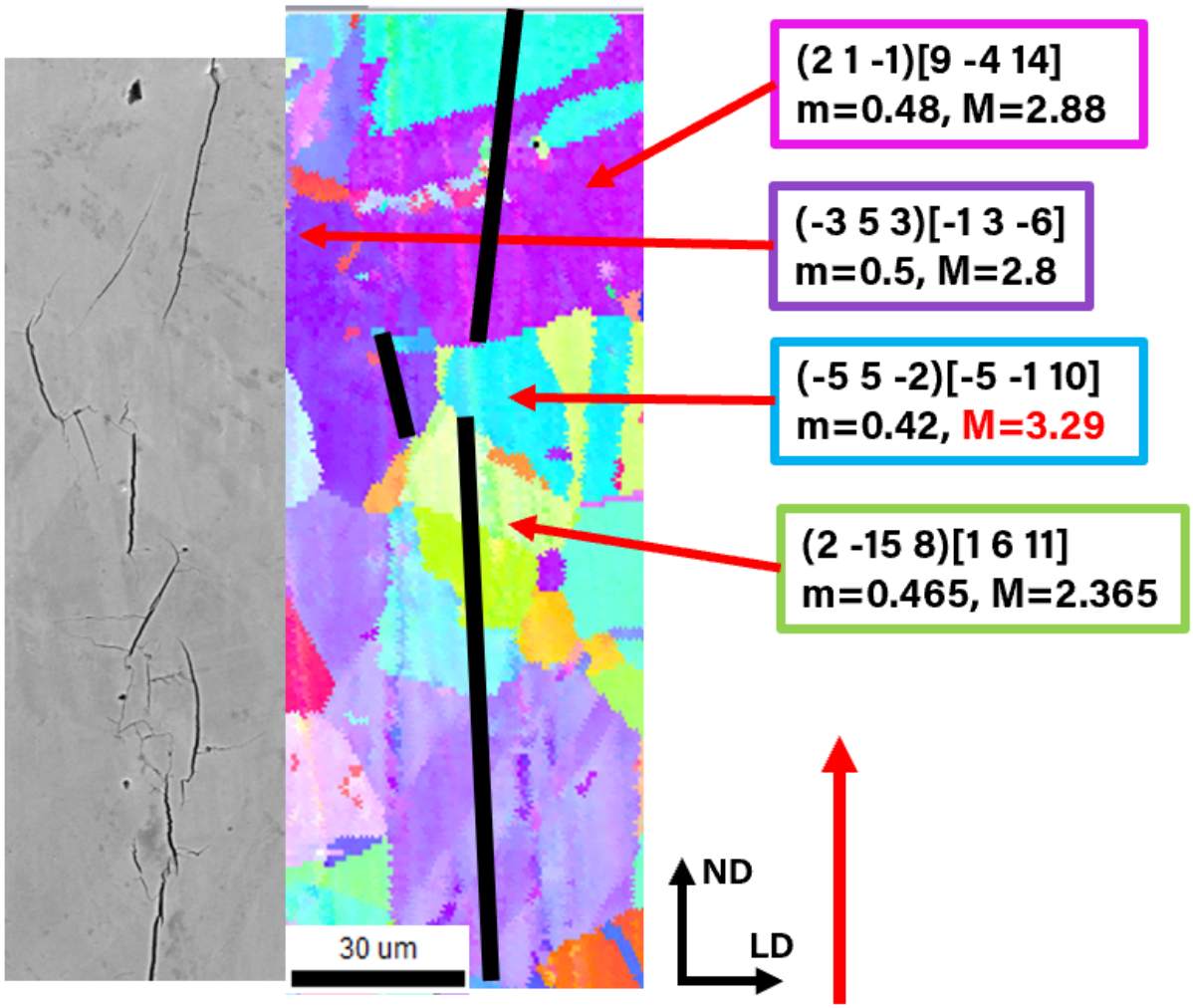

Figure 4.17. EBSD and SEM map of C68 crack with grain orientation, Schmid factor, and Taylor factor labeled. Notice the crack detour circled on the top

5. DISCUSSION

5.1 Intergranular Strain and Stress Mismatch Controlled Cracking

SCC typically grows along the slip plane as energy expenditure is minimized [35][34][38][17]. TGSCC has been shown to be driven by localized plastic deformation with environmental corrosion assistance [41][42]. Criterion of slip system activation by dislocation motion and pile-up against obstacles, either Lomer locks [36] or, in this thesis, grain boundaries, is assessed below as represented by Schmid and Taylor factor.

Schmid factor is the direct parameter that determines the shear stress required to activate the most active slip system, assuming isostress equilibrium [58], as shown in Equation 5.1 [59].

$$\sigma_y = \frac{\tau_{CRSS}}{m} \tag{5.1}$$

where σ_y is yield strength of the grain, and τ_{CRSS} is the critical resolved shear stress on the active slip plane. High Schmid factor indicates less stress is required to provide sufficient shear stress on the active slip system [59]. Grains with high Schmid factor are oriented with easy slip step to break passive film to initiate brittle cracking across GB [7][60][27].

On the contrary, Taylor factor is derived based on the assumption of isostrain condition in polycrystalline materials [58]. It is typically used to correlate macroscopic flow stress and the resolved shear stress, assuming multiple slip systems share same shear stress as alternative to each other [61].

$$M = \frac{d\gamma}{d\epsilon_x} = \frac{\sigma_x}{\tau} \tag{5.2}$$

where σ is the macroscopic flow stress, ϵ is the grain strain, γ is the shear strain on each slip plane, and τ is the shear stress on active slip planes.

5.1.1 Crack Propagation

As shown in last chapter, from Figure 4.9a and 4.10a, direct correlation between initiation and Schmid/Taylor factor alone is not found. However, from Figure 4.8, correlation between crack propagation and m/M mismatch is shown. Most the crack propagation grain pairs are allocated in the the second and forth quadrants of the map, indicating a "hard $\leftrightarrow$ soft" pair

preference. Both Schmid factor and Taylor factor describe plastic deformation in the grain [85][59].

Low Taylor factor indicates that less shear strain is required to accommodate the overall tensile strain [62]. Thus, crack propagation is facilitated with reduced dislocation pile-up and localized strain at the grain boundary before a grain with low M. Meanwhile, because of the isostrain assumption, Taylor factor can also be used to evaluate grain specific stress in terms of macroscopic stress, as demonstrated in Equation 5.3.

$$\sigma_{hkl} = \frac{M_{hkl}}{M_{average}} \cdot \sigma_{average} \tag{5.3}$$

where σ_{hkl} is grain specific stress, M_{hkl} is the Taylor factor of the grain, and $M_{average}$ is the average Taylor factor for the randomly oriented sample, which is 3.067 for FCC polycrystalline as calculated by Taylor [59]. Grains with high Taylor factor experience higher stress than its surroundings, leading to greater strain hardening and develops a higher dislocation density to maintain strain compatibility with the neighbouring grains [63][59][64].

Thus, as the crack propagation pairs are dominantly "hard $\leftrightarrow$ soft" combination, crack propagation mechanism across GB is different with "hard $\rightarrow$ soft" and "soft $\rightarrow$ hard" condition. In the "hard $\rightarrow$ soft" scenario, high Schmid factor in the soft grain indicates higher shear stress on the slip plane and low Taylor factor indicates less shear stress is required for the active slip systems to be activated. Thus, it is easy for the soft grain to nucleate dislocations and form slip steps at the crack tip [35][36][27]. On the other hand, in the "soft $\rightarrow$ hard" scenario, based on the observation that most cracks stop at GB and crack branch intersections start and end at GB, it is assumed crack rate is decreased and "paused" at the GB, while a speed competition between three factors for crack propagation towards high M grains is postulated:

1. Dislocation nucleation and motion are driven by stress in the high M grain to enter and interact with plastic zone ahead of crack tip [43][87].

2. Aggregation of chemical species, e.g. Chloride ion, or hydrogen adsorption reduce the critical energy required for crack tip opening [88][36].

3. Dislocation motion and emission in surrounding softer (high m and low M) grains other than the hard grain at the crack front.

In the first case, since high Taylor factor grains deform by stress concentration and strain hardening, hardened region is susceptible to brittle fracture and local yielding when dislocation is injected [63][64]. As crack pauses in front of a high M receiving grain, dislocation piles up in the cracked high m grain and intensifies the local strain at the GB. If case 1 wins with faster dislocation pile-up rate, crack will propagate through the GB receiving original path. In the second case, when crack blunts as the propagation rate decreases, sufficient corrosive ions (Cl^-) or hydrogen are transported to the crack tip to maintain SCC electrochemical condition, e.g., electroneutrality, local acidity, and electro-potential [89][7][90][91]. Adsorbed hydrogen can also act as a pin point for dislocation to intensify local stress within the grain [37]. If case 2 wins with sufficient ion/mass migration rate, crack will also propagate through the GB receiving original path. In the third case, when adjacent grains have sufficient dislocation accumulation and slip system is activated to form slip step, crack will propagate through the adjacent grain, detours around the hard grain. One thing to notice is that SCC is 3D indeed, but the current EBSD only shows a 2D view on one specific plane. Thus, in the EBSD map of detour cases, e.g., Figure 4.17, crack detour looks like a discontinuous separation from the main path.

In Figure 4.8, branch intersection also concentrates in the second and forth quadrants, demonstrating the 3D nature of crack propagation along slip planes. These discontinuous branches are caused by the shear of ligaments connecting coplanar crack branches that are not fully developed laterally yet [92][93][77]. In the case where the current viewing plane is offset from the intersection plane (X-Y plane) of Figure 5.1 by distance h in the -z direction, the distance between two adjacent crack coalescence on current plane can be estimated by D = h*sinα. However, with limited access to 2D EBSD map, it is hard to confirm the 3D propagation pattern of these discontinuous cracks. 3D X-ray tomography via 3D FIB slicing will help further investigate this phenomena. Yet, it is observed that all of the intersection start and end at GB, indicating cracks pause at GB waiting for propagation criteria to be met, as discussed earlier.

5.1.2 Crack Stop

Other than propagation, most cracks are found to "stop" at the GB exactly when corrosion experiment is terminated. From the mismatch map (Figure 4.8), it is observed that crack "stop" cases concentrate in the second quadrant, which is soft → hard grain pair. This further validates the earlier assumption that crack pauses at GB with harder grain (low m, high M) and the "waiting time" before postulated competition is finished. The two outlier of the stop case may be attributed to large α and β between the crack plane and slip plane in receiving grain, which retards crack propagation [94].

5.1.3 Crack Detour

C68: Figure 4.17 is an example for crack detour from its expected propagation path. The cyan (-5 5 -2) grain is expected to be the next grain where the crack propagation through from the green (2 -15 8) grain. However, as marked by black crack path, crack avoids the cyan (-5 5 -2) grain. In stead, it takes an alternative route through the purple (-3 5 3) grain and returns back to the original path in the pink (2 1 -1) grain.

It is noticed that the cyan (-5 5 -2) grain has higher Taylor factor than all of the surrounding grains. Equation 5.3 indicates that stress in a specific grain is inversely related with its Taylor factor because of the isostrain constraint by its surrounding grains. Thus, it is expected that cyan (-5 5 -2) grain experiences has lower stress within and less shear stress for its slip system be to activated, compared with its neighbors. As described in case 3 in section 5.1, dislocation nucleation and emission in the neighbor purple (m=0.5, M=2.8) grain is faster than the hardening of the cyan (-5 5 -2) grain and dissolution at GB between the green and cyan grains. Thus, crack detours in the adjacent purple grain, in stead of the cyan grain. While SCC is 3D in nature, EBSD can only provide 2D view of the crack structure on the plane exposed. Thus, it's very likely that in the TD direction, crack are still connected and propagating in the original green (2 -15 8) ↔ pink (2 1 -1) path. In the current LD-ND plane, crack is confronted by the high M cyan (-5 5 -2) grain that has insufficient shear stress to activate slip systems, and thus detours through neighbor grains around it.

5.1.4 Crack Jump

Crack jump potentially belongs to the same category of crack detour phenomena. The crack jump observed in Figure 4.14 is attributed to the limited stress at the GB between the cyan (14 -5 -12) and orange (1 27 4) grains. The two grains have similar Schmid factor, but the Taylor factor for the orange grain is much higher than the cyan one. Thus, the softer orange (1 27 4) grain experience less shear stress for its slip system be to activated, when crack tip approaches the GB. Besides, On the current plane, only a dendrite of the orange grain is enclosed in the cyan grain, suppressing dislocation motion and slip activation. Thus, it is reasonable to presume that crack propagation passes around the orange grain and follows the same slip system within the cyan grain.

In summary, inter-grain m and M mismatch intensifies the local strain and stress in front of the crack tip, leading to dislocation motion and emission along slip systems and plastic deformation.

5.2 Schmid and Taylor Factor Controlled Crack Propagation Within Grain

The combination of Schmid factor and Taylor factor not only explains crack path across GB, but also within grains.

Due to the availability of slip systems at GB, depending on the α and β between the crack and GB, slip system with highest Schmid factor may not be readily activated and crack crosses GB along the secondary slip system. However, as crack propagates within the grain, when it encounters the slip system exposed to higher shear, crack will twist and kink to follow the dominant direction .

When Taylor factor is high, it indicates that more stress is required for multiple slip system to be activated and become alternative to each other [62][85]. In such grains, it is easier for crack to encounter slip systems with similar shear along its propagation path once local stress within grain is sufficiently high. Thus, it is easier for crack to show zig-zag or twisted appearance in high-M grains than low-M grains. The cyan (14 -5 -12) grain in Figure 4.14 has low Taylor factor (2.5) and high Schmid factor (0.46) combination. From the SEM image, it is observed that crack has very brittle appearance, indicating crack follows single

activated slip system with no alternation along the path. Similar trend is observed in the navy (2 3 4) grain (m=0.5, M=2.7) in Figure 4.15 that the crack path is brittle and straight too. On the contrary, in the cyan (1 2 2) grain (m=0.43, M=3.64) in Figure 4.16, and navy (-3 4 2), (-2 4 -3) grains (m=0.45, M=3.03), (m=0.43, M=3.05) in Figure 4.15, cracks show striation and river pattern [95] with secondary microcrack branches.

However, there are still outliers in the mismatch map, e.g., for crack stop at GB and branch intersection. This indicates that local strain and stress incompatibility, as represented by Schmid factor and Taylor factor, are not sufficient to comprehensively describe and predict SCC behaviors. Thus, other factors must be considered when evaluating SCC phenomena.

5.3 Grain Orientation

As SCC involves heavily with plasticity deformation, anisotropic property of each grain plays an important role in plastic behavior and crack growth [96][93]. When combining Figure 4.6b with 4.7a and 4.7b, it is seen that both Schmid factor and Taylor factor are noticeably different between the $\{001\} - \{111\}$ pair for IGSCC initiation. This is further confirmed in the mismatch map in Figure 4.8. In addition, $\{011\}$ has the lowest planar density ($\frac{0.177}{R_2}$) and is thus the softest orientation family in FCC structure [86]. On the contrary, $\{001\}$ and $\{111\}$ have higher planar density ($\frac{0.25}{R_2}$ and $\frac{0.29}{R_2}$) and are harder grains [97]. Thus, $\{001\}$ and $\{111\}$ grains are not as good at accommodate local stress as $\{011\}$ and intensify the local strain. Difference of the deformation properties between the adjacent grains led to local strain gradient and higher grain boundary energy, increasing the susceptibility of GB for SCC [98][99]. Because IGSCC is suppressed by the ultra-low carbon impurity content, mechanical properties, e.g., strain incompatibility, between adjacent grains are attributed to the IGSCC in current results of this thesis [100] [62][101].

From Figure 4.6c, it is observed that most propagation happens in pairs along the $\{001\} \leftrightarrow \{111\}$ direction. When combined with Figure 4.7a and 4.7b, both Schmid factor and Taylor factor are different between the propagation pairs marked by arrows in Figure 4.6c along $\{001\} \leftrightarrow \{111\}$ direction. As discussed in section 5.1, inter-grain m and M mismatch intensifies the local strain and stress in front of the crack tip, leading to dislocation motion and emission along slip systems and plastic deformation in the high m grain. Thus, it is

expected that grain pairs between {001} and {111} orientations ease the crack propagation, compared with combinations along other orientations.

On the contrary, crack initiation on the surface doesn't have the constraint of slip system activation position approaching crack front. When the convex side of bent sample is loaded with uniaxial stress, grains on the sample surface experience different level of local stress, depending on the Taylor factor of each grain [59]. As Equation 2.5 indicates, stress in a specific grain is inversely related with its Taylor factor because of the isostrain constraint by its surrounding grains [59]. From Figure 4.7b, {011} and {111} regions have higher Taylor factor than the {001} region. When comparing with Figure 4.6b, it is noticed that most of the TGSCC initiation grains fall in the middle (> 2.9) and high M (> 3.3) region. Thus, higher grain specific stress increases the opportunity for slip to activate and break surface passive film, which triggers the SCC initiation.

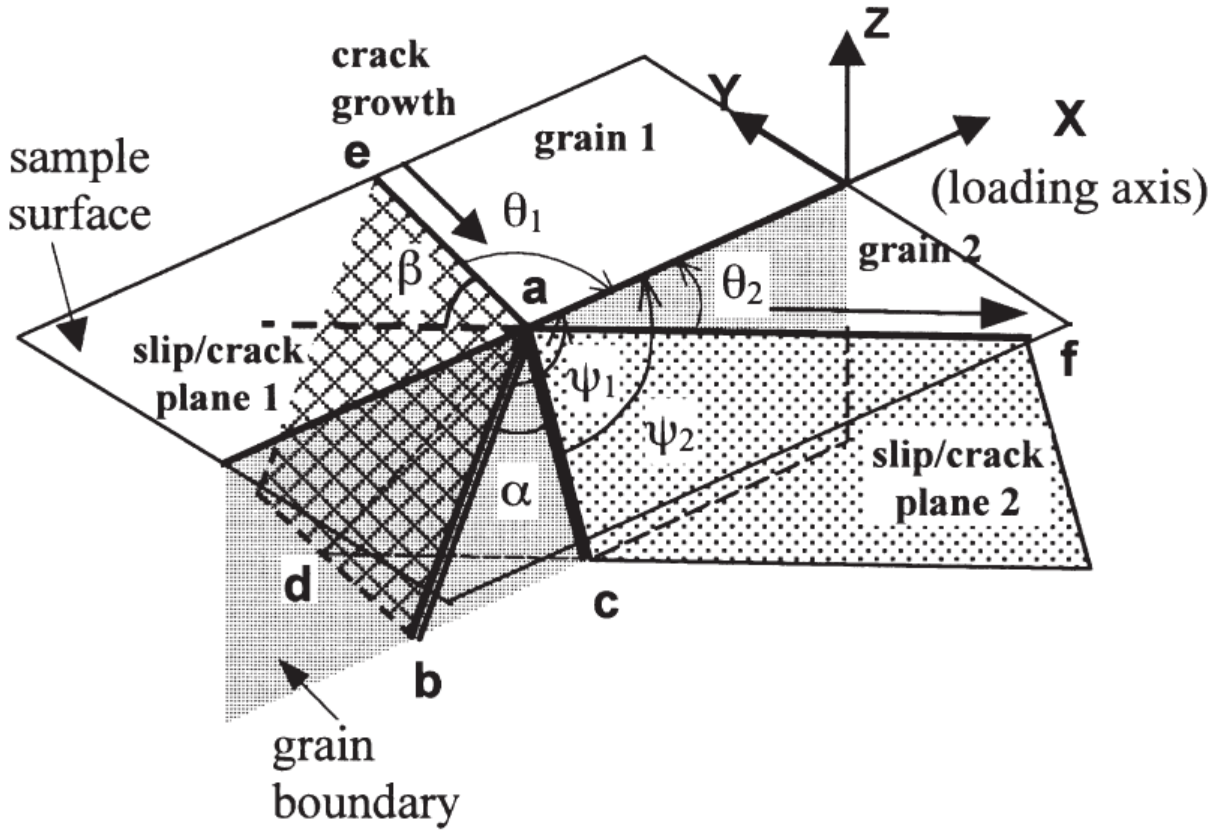

Figure 5.1. Schematic illustration of the crystallography system for crack plane deflection calculation

6. CONCLUSIONS AND FUTURE WORK

SCC crack propagation is a complex problem that involves energy (hydrostatic), stress and strain (fracture mechanics), grain orientation (α and β), and chemical (hydrogen and chloride effect), temperature, from Staehle's model [102]. Through this thesis, it has been shown that slip system controlled local strain, stress, and structure anisotropy can explain TGSCC initiation and propagation behavior from a mechanical perspective. Crack slows down at grain boundary and waits for one of the following three propagation criteria to be met: a. Mechanical fracture from dislocation pile-up induced plasticity; b. corrosion ion species reduce cohesion energy of atoms at crack tip; c. slip step formation in surrounding grains resulting alternative propagation path. However, no quantified model of this propagation criteria has been proposed systematically. Combined with new advances of fracture mechanics in micron and sub-micron level, the energy and stress balance controlling SCC crack propagation is worth further investigation and development.

Main takeaways from this thesis are:

1. Similar to local strain incompatibility in adjacent grain pairs in IGSCC, TGSCC crack propagation is also controlled by local strain and stress state on GB and within cracked grains, competing with other factors, e.g., crack plane inclination, surface boundary modification by electrochemical reactions.

2. Schmid factor and Taylor factor can qualitatively describe the interaction between slip system and crack path in both macroscopic and microscopic manner.

3. Accurate and comprehensive quantitative modeling of preferential crack propagation pattern involves various aspects being considered, such as mechanical (local strain and stress) and crystallographic, as discussed in this thesis, and many other described by Staehle [8]

As SCC involves many different factors, taking all of these factors into account when predicting and comprehensively modeling SCC is almost impossible. To further comprehensively understand and predict SCC, more in-depth numerical modeling and simulations around all

aspects, together with the power of non-linear optimization, can help us to systematically understand SCC from multi-dimensions.

REFERENCES

[1] R. W. Staehle. (1969). Fundamental aspects of stress corrosion cracking : Proceedings of conference september 11-15, 1967, the ohio state university department of metallurgical engineering, undefined, [Online]. Available: /paper/Fundamental-aspects-of-stress-corrosion-cracking-%3A-Staehle/cbfa06abeefb47487813d5119b93873b0f00e44a.

[2] O. M. Alyousif and R. Nishimura, "The stress corrosion cracking behavior of austenitic stainless steels in boiling magnesium chloride solutions," *Corrosion Science*, vol. 49, no. 7, pp. 3040–3051, Jul. 1, 2007, ISSN: 0010-938X. DOI: 10.1016/j.corsci.2006.12.023. [Online]. Available: http://www.sciencedirect.com/science/article/pii/S0010938X07000248.

[3] G. S. Was and T. R. Allen, "Chapter 6 - corrosion issues in current and next-generation nuclear reactors," in *Structural Alloys for Nuclear Energy Applications*, G. R. Odette and S. J. Zinkle, Eds., Boston: Elsevier, Jan. 1, 2019, pp. 211–246, ISBN: 978-0-12-397046-6. DOI: 10.1016/B978-0-12-397046-6.00006-X. [Online]. Available: http://www.sciencedirect.com/science/article/pii/B978012397046600006X.

[4] C. Padovani, F. King, C. Lilja, D. Féron, S. Necib, D. Crusset, V. Deydier, N. Diomidis, R. Gaggiano, T. Ahn, P. G. Keech, D. D. Macdonald, H. Asano, N. Smart, D. S. Hall, H. Hänninen, D. Engelberg, J. J. Noël, and D. W. Shoesmith, "The corrosion behaviour of candidate container materials for the disposal of high-level waste and spent fuel–a summary of the state of the art and opportunities for synergies in future r&d," *Corrosion Engineering Science and Technology*, vol. 52, pp. 227–231, Apr. 2017, Publisher: Taylor and Francis Ltd., ISSN: 17432782. DOI: 10.1080/1478422X.2017.1356973.

[5] F. Hua, P. Pasupathi, N. Brown, and K. Mon, "Some materials degradation issues in the u.s. high-level nuclear waste repository study (the yucca mountain project)," Yucca Mountain Project, Las Vegas, Nevada, Sep. 2005. DOI: 10.2172/840143. [Online]. Available: http://www.osti.gov/servlets/purl/840143-ATNige/webviewable/.

[6] D. A. Jones. (1992). Principles and prevention of corrosion, CERN Document Server. ISBN: 9780029464397 Publisher: Macmillan, [Online]. Available: https://cds.cern.ch/record/245067.

[7] R. N. Parkins, "8.1 - mechanisms of stress-corrosion cracking," in *Corrosion (Third Edition)*, L. L. Shreir, R. A. Jarman, and G. T. Burstein, Eds., Oxford: Butterworth-Heinemann, Jan. 1, 1994, 8:3–8:31, ISBN: 978-0-08-052351-4. DOI: 10.1016/B978-0-08-052351-4.50064-9. [Online]. Available: http://www.sciencedirect.com/science/article/pii/B9780080523514500649.

[8] R. W. Staehle, "Bases for predicting the earliest penetrations due to SCC for alloy 600 on the secondary side of PWR steam generators (NUREG/CR-6737)," Sep. 2001, [Online]. Available: https://www.nrc.gov/reading-rm/doc-collections/nuregs/contract/cr6737/.

[9] P. Marcus, *Corrosion Mechanisms in Theory and Practice*. CRC Press, Aug. 2011, Publication Title: Corrosion Mechanisms in Theory and Practice. DOI: 10.1201/b11020.

[10] W. L. Williams, *Stress-Corrosion Cracking: A Review of Current Status*, 7, vol. 17, 340t–344t, ISSN: 0010-9312 Publication Title: CORROSION. DOI: 10.5006/0010-9312-17.7.92.

[11] R. H. Jones, *Stress Corrosion Cracking: Materials Performance and Evaluation*. Materials Park, OH, UNITED STATES: ASM International, 2017, ISBN: 978-1-62708-119-1. [Online]. Available: http://ebookcentral.proquest.com/lib/purdue/detail.action?docID=5340327.

[12] G. S. Was, *Fundamentals of Radiation Materials Science*. New York, NY: Springer New York, 2017, ISBN: 978-1-4939-3436-2 978-1-4939-3438-6. DOI: 10.1007/978-1-4939-3438-6. [Online]. Available: http://link.springer.com/10.1007/978-1-4939-3438-6.

[13] K. Sadananda and A. K. Vasudevan, "Review of environmentally assisted cracking," *Metallurgical and Materials Transactions A*, vol. 42, no. 2, pp. 279–295, Feb. 1, 2011, ISSN: 1543-1940. DOI: 10.1007/s11661-010-0472-3. [Online]. Available: https://doi.org/10.1007/s11661-010-0472-3.

[14] J. Congleton, "8.3 - stress-corrosion cracking of stainless steels," in *Corrosion (Third Edition)*, L. L. Shreir, R. A. Jarman, and G. T. Burstein, Eds., Oxford: Butterworth-Heinemann, Jan. 1, 1994, 8:52–8:83, ISBN: 978-0-08-052351-4. DOI: 10.1016/B978-0-08-052351-4.50066-2. [Online]. Available: http://www.sciencedirect.com/science/article/pii/B9780080523514500662.

[15] M. G. Fontana and N. D. Greene, *Corrosion Engineering*. McGraw-Hill, Oct. 26, 2018, Accepted: 2018-11-07T03:43:30Z, ISBN: 978-0-07-021461-3. [Online]. Available: https://modps71.lib.kmutt.ac.th/xmlui//handle/123456789/310.

[16] R. C. Newman, "Stress-corrosion cracking mechanisms," in *Corrosion Mechanisms in Theory and Practice*, CRC Press, 2011, pp. 511–556.

[17] R. C. NEWMAN and R. P. M. PROCTER, "Stress corrosion cracking: 1965–1990," *British Corrosion Journal*, vol. 25, no. 4, pp. 259–270, Jan. 1, 1990, Publisher: Taylor & Francis _eprint: https://doi.org/10.1179/000705990799156373, ISSN: 0007-0599.

DOI: 10.1179/000705990799156373. [Online]. Available: https://doi.org/10.1179/000705990799156373.

[18] A. Turnbull, "Stress corrosion cracking: Mechanisms," in *Encyclopedia of Materials: Science and Technology*, K. H. J. Buschow, R. W. Cahn, M. C. Flemings, B. Ilschner, E. J. Kramer, S. Mahajan, and P. Veyssière, Eds., Oxford: Elsevier, Jan. 1, 2001, pp. 8886–8891, ISBN: 978-0-08-043152-9. DOI: 10.1016/B0-08-043152-6/01598-9. [Online]. Available: http://www.sciencedirect.com/science/article/pii/B0080431526015989.

[19] K. R. Trethewey, "Some observations on the current status in the understanding of stress-corrosion cracking of stainless steels," *Materials & Design*, vol. 29, no. 2, pp. 501–507, Jan. 1, 2008, ISSN: 0261-3069. DOI: 10.1016/j.matdes.2007.02.001. [Online]. Available: http://www.sciencedirect.com/science/article/pii/S0261306907000453.

[20] R. Mears, R. Brown, and E. Dix, "A generalized theory of stress corrosion of alloys," *Symposium on Stress-Corrosion Cracking of Metals*, Jan. 1945, Publisher: ASTM International. DOI: 10.1520/STP42581S. [Online]. Available: http://www.astm.org/DIGITAL_LIBRARY/STP/PAGES/STP42581S.htm.

[21] H. Logan, "Film-rupture mechanism of stress corrosion," *Journal of Research of the National Bureau of Standards*, vol. 48, no. 2, p. 99, Feb. 1952, Publisher: National Institute of Standards and Technology (NIST), ISSN: 0091-0635. DOI: 10.6028/jres.048.013.

[22] D. A. Vermilyea, "A theory for the propagation of stress corrosion cracks in metals," *Journal of The Electrochemical Society*, vol. 119, no. 4, p. 405, Apr. 1, 1972, Publisher: IOP Publishing, ISSN: 1945-7111. DOI: 10.1149/1.2404217. [Online]. Available: https://iopscience.iop.org/article/10.1149/1.2404217/meta.

[23] P. L. Andresen and F. Peter Ford, "Life prediction by mechanistic modeling and system monitoring of environmental cracking of iron and nickel alloys in aqueous systems," *Materials Science and Engineering: A*, Workshop on the Mechanics and Physics of Crack Growth: Application to Life Prediction, vol. 103, no. 1, pp. 167–184, Aug. 1, 1988, ISSN: 0921-5093. DOI: 10.1016/0025-5416(88)90564-2. [Online]. Available: http://www.sciencedirect.com/science/article/pii/0025541688905642.

[24] P. L. Andresen and F. P. Ford, "Fundamental modeling of environmental cracking for improved design and lifetime evaluation in BWRs," *International Journal of Pressure Vessels and Piping*, vol. 59, no. 1, pp. 61–70, Jan. 1, 1994, ISSN: 0308-0161. DOI: 10.1016/0308-0161(94)90142-2. [Online]. Available: http://www.sciencedirect.com/science/article/pii/0308016194901422.

[25] R. B. Rebak and Z. Szklarska-Smialowska, "The mechanism of stress corrosion cracking of alloy 600 in high temperature water," *Corrosion Science*, vol. 38, no. 6, pp. 971–988, Jun. 1, 1996, ISSN: 0010-938X. DOI: 10.1016/0010-938X(96)00183-7. [Online]. Available: http://www.sciencedirect.com/science/article/pii/0010938X96001837.

[26] C. D. Thompson, H. T. Krasodomski, N. Lewis, and G. L. Makar, "Prediction of pure water stress corrosion cracking (PWSCC) in nickel base alloys using crack growth rate models," Knolls Atomic Power Lab., KAPL-P–000005, 1995. [Online]. Available: http://inis.iaea.org/Search/search.aspx?orig_q=RN:30046938.

[27] T. J. Smith and R. W. Staehle, "Role of slip step emergence in the early stages of stress corrosion cracking in face centered iron-nickel-chromium alloys," *CORROSION*, vol. 23, no. 5, pp. 117–129, May 1, 1967, Publisher: NACE International, ISSN: 0010-9312. DOI: 10.5006/0010-9312-23.5.117. [Online]. Available: https://www.corrosionjournal.org/doi/abs/10.5006/0010-9312-23.5.117.

[28] R. W. Stahle, J. Hochmann, R. D. McCright, J. E. Slater, and S. R. Shatynski, "Stress corrosion cracking and hydrogen embrittlement of iron base alloys," *Journal of The Electrochemical Society*, vol. 126, no. 5, pp. 215C–215C, 1979, Publisher: The Electrochemical Society.

[29] O. F. Aly and M. M. Neto, "THE SLIP-STEP DISSOLUTION AND FILM RUPTURE MODEL - a CRITICAL REVIEW AND AN ALTERNATIVE MODELING PROPOSAL," p. 10, 2013.

[30] C. Edeleanu and A. J. Forty, "Some observations on the stress-corrosion cracking of -brass and similar alloys," *The Philosophical Magazine: A Journal of Theoretical Experimental and Applied Physics*, vol. 5, no. 58, pp. 1029–1040, Oct. 1, 1960, Publisher: Taylor & Francis _eprint: https://doi.org/10.1080/14786436008235881, ISSN: 0031-8086. DOI: 10.1080/14786436008235881. [Online]. Available: https://doi.org/10.1080/14786436008235881.

[31] J. A. Beavers and E. N. Pugh, "The propagation of transgranular stress-corrosion cracks in admiralty metal," *Metallurgical Transactions A*, vol. 11, no. 5, pp. 809–820, May 1980, ISSN: 0360-2133, 1543-1940. DOI: 10.1007/BF02661210. [Online]. Available: http://link.springer.com/10.1007/BF02661210.

[32] K. Sieradzki and R. C. Newman, "Brittle behavior of ductile metals during stress-corrosion cracking," *Philosophical Magazine A*, vol. 51, no. 1, pp. 95–132, Jan. 1, 1985, Publisher: Taylor & Francis _eprint: https://doi.org/10.1080/01418618508245272, ISSN: 0141-8610. DOI: 10.1080/01418618508245272. [Online]. Available: https://doi.org/10.1080/01418618508245272.

[33] L. Shreir, *Corrosion: Corrosion control, with a section on corrosion testing, by FL Laque*. G. Newnes, 1963, vol. 2.

[34] T. Magnin, R. Chieragatti, and R. Oltra, "Mechanism of brittle fracture in a ductile 316 alloy during stress corrosion," *Acta Metallurgica et Materialia*, vol. 38, no. 7, pp. 1313–1319, Jul. 1, 1990, ISSN: 0956-7151. DOI: 10.1016/0956-7151(90)90203-S. [Online]. Available: http://www.sciencedirect.com/science/article/pii/095671519090203S.

[35] T. Magnin, A. Chambreuil, and B. Bayle, "The corrosion-enhanced plasticity model for stress corrosion cracking in ductile fcc alloys," *Acta Materialia*, vol. 44, no. 4, pp. 1457–1470, Apr. 1, 1996, ISSN: 1359-6454. DOI: 10.1016/1359-6454(95)00301-0. [Online]. Available: http://www.sciencedirect.com/science/article/pii/1359645495003010.

[36] J. P. Chateau, D. Delafosse, and T. Magnin, "1 numerical simulations of hydrogen–dislocation interactions in fcc stainless steels.: Part i: Hydrogen–dislocation interactions in bulk crystals," *Acta Materialia*, vol. 50, no. 6, pp. 1507–1522, Apr. 2, 2002, ISSN: 1359-6454. DOI: 10.1016/S1359-6454(02)00008-3. [Online]. Available: http://www.sciencedirect.com/science/article/pii/S1359645402000083.

[37] J. P. Chateau, D. Delafosse, and T. Magnin, "2 numerical simulations of hydrogen–dislocation interactions in fcc stainless steels.: Part II: Hydrogen effects on crack tip plasticity at a stress corrosion crack," *Acta Materialia*, vol. 50, no. 6, pp. 1523–1538, Apr. 2, 2002, ISSN: 1359-6454. DOI: 10.1016/S1359-6454(02)00009-5. [Online]. Available: http://www.sciencedirect.com/science/article/pii/S1359645402000095.

[38] L. Zhu, Y. Yan, J. Li, L. Qiao, Z. Li, and A. A. Volinsky, "Stress corrosion cracking at low loads: Surface slip and crystallographic analysis," *Corrosion Science*, vol. 100, pp. 619–626, Nov. 1, 2015, ISSN: 0010-938X. DOI: 10.1016/j.corsci.2015.08.040. [Online]. Available: http://www.sciencedirect.com/science/article/pii/S0010938X1530072X.

[39] R. N. Parkins, "Stress corrosion spectrum," *British Corrosion Journal*, Nov. 20, 2013, Publisher: Taylor & Francis. DOI: 10.1179/000705972798323350. [Online]. Available: https://www-tandfonline-com.ezproxy.lib.purdue.edu/doi/abs/10.1179/000705972798323350.

[40] R. W. Staehle and J. A. Gorman, "2 quantitative assessment of submodes of stress corrosion cracking on the secondary side of steam generator tubing in pressurized water reactors: Part 2," *CORROSION*, vol. 60, no. 1, pp. 5–63, Jan. 1, 2004, Publisher: NACE International, ISSN: 0010-9312. DOI: 10.5006/1.3299232. [Online]. Available: https://corrosionjournal.org/doi/abs/10.5006/1.3299232.

[41] J. X. Li, W. Y. Chu, Y. B. Wang, and L. J. Qiao, "In situ TEM study of stress corrosion cracking of austenitic stainless steel," *Corrosion Science*, vol. 45, no. 7, pp. 1355–1365, Jul. 1, 2003, ISSN: 0010-938X. DOI: 10.1016/S0010-938X(02)00225-

1. [Online]. Available: http://www.sciencedirect.com/science/article/pii/S0010938X02002251.

[42] K. Lian and E. I. Meletis, "Environment-induced deformation localization during transgranular stress corrosion cracking," *CORROSION*, vol. 52, no. 5, pp. 347–355, May 1, 1996, Publisher: NACE International, ISSN: 0010-9312. DOI: 10.5006/1.3292122. [Online]. Available: https://corrosionjournal.org/doi/10.5006/1.3292122.

[43] T. L. Anderson, *Fracture Mechanics : Fundamentals and Applications, Fourth Edition*. CRC Press, Mar. 3, 2017, ISBN: 978-1-315-37029-3. DOI: 10.1201/9781315370293. [Online]. Available: https://www.taylorfrancis.com/books/9781315370293.

[44] X. Sun, J. Xu, and Y. Li, "Hydrogen permeation behavior in metastable austenitic stainless steels 321 and 304," *Acta Metallurgica*, vol. 37, no. 8, pp. 2171–2176, Aug. 1, 1989, ISSN: 0001-6160. DOI: 10.1016/0001-6160(89)90142-9. [Online]. Available: http://www.sciencedirect.com/science/article/pii/0001616089901429.

[45] S. Ghosh and V. Kain, "Effect of surface machining and cold working on the ambient temperature chloride stress corrosion cracking susceptibility of AISI 304l stainless steel," *Materials Science and Engineering: A*, vol. 527, no. 3, pp. 679–683, Jan. 15, 2010, ISSN: 0921-5093. DOI: 10.1016/j.msea.2009.08.039. [Online]. Available: http://www.sciencedirect.com/science/article/pii/S092150930900968X.

[46] G. R. Argade, N. Kumar, and R. S. Mishra, "Stress corrosion cracking susceptibility of ultrafine grained al–mg–sc alloy," *Materials Science and Engineering: A*, vol. 565, pp. 80–89, Mar. 10, 2013, ISSN: 0921-5093. DOI: 10.1016/j.msea.2012.11.066. [Online]. Available: http://www.sciencedirect.com/science/article/pii/S0921509312016188.

[47] K. D. Ralston and N. Birbilis, "Effect of grain size on corrosion: A review," *CORROSION*, vol. 66, no. 7, pp. 075005–075005–13, Jul. 2010, ISSN: 0010-9312, 1938-159X. DOI: 10.5006/1.3462912. [Online]. Available: http://corrosionjournal.org/doi/10.5006/1.3462912.

[48] W. Li and D. Y. Li, "EFFECT OF GRAIN SIZE ON THE ELECTRON WORK FUNCTION OF cu AND al," *Surface Review and Letters*, vol. 11, no. 2, pp. 173–178, Apr. 1, 2004, Publisher: World Scientific Publishing Co., ISSN: 0218-625X. DOI: 10.1142/S0218625X04006025. [Online]. Available: https://www.worldscientific.com/doi/abs/10.1142/S0218625X04006025.

[49] S. J. Splinter, R. Rofagha, N. S. McIntyre, and U. Erb, "XPS characterization of the corrosion films formed on nanocrystalline ni–p alloys in sulphuric acid," *Surface and Interface Analysis*, vol. 24, no. 3, pp. 181–186, 1996, _eprint: https://onlinelibrary.wiley.com/doi/pdf/9918%28199603%2924%3A3%3C181%3A%3AAID-SIA92%3E3.0.CO%3B2-N, ISSN: 1096-

9918. DOI: 10.1002/(SICI)1096-9918(199603)24:3<181::AID-SIA92>3.0.CO;2-N. [Online]. Available: https://onlinelibrary.wiley.com/doi/abs/10.1002/%28SICI%291096-9918%28199603%2924%3A3%3C181%3A%3AAID-SIA92%3E3.0.CO%3B2-N.

[50] G. Meric de Bellefon and J. C. van Duysen, "Tailoring plasticity of austenitic stainless steels for nuclear applications: Review of mechanisms controlling plasticity of austenitic steels below 400 °c," *Journal of Nuclear Materials*, vol. 475, pp. 168–191, Jul. 1, 2016, ISSN: 0022-3115. DOI: 10.1016/j.jnucmat.2016.04.015. [Online]. Available: http://www.sciencedirect.com/science/article/pii/S0022311516301295.

[51] T. S. Byun, "On the stress dependence of partial dislocation separation and deformation microstructure in austenitic stainless steels," *Acta Materialia*, vol. 51, no. 11, pp. 3063–3071, Jun. 27, 2003, ISSN: 1359-6454. DOI: 10.1016/S1359-6454(03)00117-4. [Online]. Available: http://www.sciencedirect.com/science/article/pii/S1359645403001174.

[52] D. T. Pierce, J. A. Jiménez, J. Bentley, D. Raabe, and J. E. Wittig, "The influence of stacking fault energy on the microstructural and strain-hardening evolution of fe–mn–al–si steels during tensile deformation," *Acta Materialia*, vol. 100, pp. 178–190, Nov. 1, 2015, ISSN: 1359-6454. DOI: 10.1016/j.actamat.2015.08.030. [Online]. Available: http://www.sciencedirect.com/science/article/pii/S1359645415006072.

[53] J. Lu, L. Hultman, E. Holmström, K. H. Antonsson, M. Grehk, W. Li, L. Vitos, and A. Golpayegani, "Stacking fault energies in austenitic stainless steels," *Acta Materialia*, vol. 111, pp. 39–46, Jun. 1, 2016, ISSN: 1359-6454. DOI: 10.1016/j.actamat.2016.03.042. [Online]. Available: http://www.sciencedirect.com/science/article/pii/S1359645416301951.

[54] A. E. Pontini and J. D. Hermida, "X-ray diffraction measurement of the stacking fault energy reduction induced by hydrogen in an AISI 304 steel," *Scripta Materialia*, vol. 37, no. 11, pp. 1831–1837, Dec. 1, 1997, ISSN: 1359-6462. DOI: 10.1016/S1359-6462(97)00332-1. [Online]. Available: http://www.sciencedirect.com/science/article/pii/S1359646297003321.

[55] P. Sofronis and H. K. Birnbaum, "Mechanics of the hydrogendashdislocationdashimpurity interactions—i. increasing shear modulus," *Journal of the Mechanics and Physics of Solids*, vol. 43, no. 1, pp. 49–90, Jan. 1, 1995, ISSN: 0022-5096. DOI: 10.1016/0022-5096(94)00056-B. [Online]. Available: http://www.sciencedirect.com/science/article/pii/002250969400056B.

[56] J. K. Tien, "Diffusion and the dislocation sweeping mechanism for hydrogen transport," *Effect of hydrogen on behavior of materials*, 1976. [Online]. Available: http://inis.iaea.org/Search/search.aspx?orig_q=RN:8321104.

[57] M. Meisnar, A. Vilalta-Clemente, M. Moody, K. Arioka, and S. Lozano-Perez, "A mechanistic study of the temperature dependence of the stress corrosion crack growth rate in SUS316 stainless steels exposed to PWR primary water," *Acta Materialia*, vol. 114, pp. 15–24, Aug. 1, 2016, ISSN: 1359-6454. DOI: 10.1016/j.actamat.2016.05.010. [Online]. Available: http://www.sciencedirect.com/science/article/pii/S135964541630338X.

[58] A. C. Poshadel and P. R. Dawson, "Role of anisotropic strength and stiffness in governing the initiation and propagation of yielding in polycrystalline solids," *Metallurgical and Materials Transactions A*, vol. 50, no. 3, pp. 1185–1201, Mar. 1, 2019, ISSN: 1543-1940. DOI: 10.1007/s11661-018-5013-5. [Online]. Available: https://doi.org/10.1007/s11661-018-5013-5.

[59] W. F. Hosford, *Mechanical Behavior of Materials*, 2nd ed. Cambridge: Cambridge University Press, 2009, ISBN: 978-0-521-19569-0. DOI: 10.1017/CBO9780511810923. [Online]. Available: https://www.cambridge.org/core/books/mechanical-behavior-of-materials/5A61AB97E367E6AE82C05D0E532D1D5A.

[60] J. Lépinoux and T. Magnin, "Stress corrosion microcleavage in a ductile f.c.c. alloy," *Materials Science and Engineering A*, vol. 164, no. 1, pp. 266–269, May 1993, Publisher: Elsevier, ISSN: 09215093. DOI: 10.1016/0921-5093(93)90675-5.

[61] G. I. Taylor, "Plastic strain in metals," *J. Inst. Metals*, vol. 62, pp. 307–324, 1938.

[62] M. D. McMurtrey, G. S. Was, L. Patrick, and D. Farkas, "Relationship between localized strain and irradiation assisted stress corrosion cracking in an austenitic alloy," *Materials Science and Engineering: A*, vol. 528, no. 10, pp. 3730–3740, Apr. 25, 2011, ISSN: 0921-5093. DOI: 10.1016/j.msea.2011.01.073. [Online]. Available: http://www.sciencedirect.com/science/article/pii/S0921509311000955.

[63] H. Beladi, I. B. Timokhina, Y. Estrin, J. Kim, B. C. De Cooman, and S. K. Kim, "Orientation dependence of twinning and strain hardening behaviour of a high manganese twinning induced plasticity steel with polycrystalline structure," *Acta Materialia*, vol. 59, no. 20, pp. 7787–7799, Dec. 1, 2011, ISSN: 1359-6454. DOI: 10.1016/j.actamat.2011.08.031. [Online]. Available: http://www.sciencedirect.com/science/article/pii/S1359645411006069.

[64] Y. Estrin, L. S. Tóth, A. Molinari, and Y. Bréchet, "A dislocation-based model for all hardening stages in large strain deformation," *Acta Materialia*, vol. 46, no. 15, pp. 5509–5522, Sep. 18, 1998, ISSN: 1359-6454. DOI: 10.1016/S1359-6454(98)00196-

7. [Online]. Available: http://www.sciencedirect.com/science/article/pii/S1359645498001967.

[65] D. Enos and C. R. Bryan, "Final report: Characterization of canister mockup weld residual stresses," SAND2016-12375R, 1335756, Dec. 1, 2016, SAND2016–12375R, 1 335 756. DOI: 10.2172/1335756. [Online]. Available: http://www.osti.gov/servlets/purl/1335756/.

[66] ASTM G39 - 99 (Reapproved 2011), "Standard practice for preparation and use of bent-beam stress-corrosion test," *ASTM International*, 2005, ISSN: 08873763. DOI: 10.1520/G0039-99R11.2.

[67] X. Wu, "On residual stress analysis and microstructural evolution for stainless steel type 304 spent nuclear fuel canisters weld joint: Numerical and experimental studies," *Journal of Nuclear Materials*, vol. 534, p. 152 131, Jun. 1, 2020, ISSN: 0022-3115. DOI: 10.1016/j.jnucmat.2020.152131. [Online]. Available: http://www.sciencedirect.com/science/article/pii/S0022311519316320.

[68] G01 Committee, "G-36: Pactice for evaluating stress-corrosion-cracking resistance of metals and alloys in a boiling magnesium chloride solution," ASTM International, G-36. DOI: 10.1520/G0036-94R18. [Online]. Available: http://www.astm.org/cgi-bin/resolver.cgi?G36-94R18.

[69] M. Scheil, "Symposium on stress corrosion cracking of metals," *AS'M-AIME*, pp. 395–410, 1944.

[70] I. B. CASALE, "Boiling temperatures of mg cl solutions -their application in stress corrosion studies," *CORROSION*, vol. 23, no. 10, pp. 314–317, 1967, ISSN: 0010-9312. DOI: 10.5006/0010-9312-23.10.314.

[71] C. Ni, "Scanning electron microscopy (SEM)," in *Encyclopedia of Tribology*, Q. J. Wang and Y.-W. Chung, Eds., Boston, MA: Springer US, 2013, pp. 2977–2982, ISBN: 978-0-387-92897-5. DOI: 10.1007/978-0-387-92897-5_1217. [Online]. Available: https://doi.org/10.1007/978-0-387-92897-5_1217.

[72] R. O. Ritchie and A. W. Thompson, *On Macroscopic and Microscopic Analyses for Crack Initiation and Crack Growth Toughness in Ductile Alloys.*

[73] B. L. Adams, S. I. Wright, and K. Kunze, "Orientation imaging: The emergence of a new microscopy," *Metallurgical Transactions A*, vol. 24, no. 4, pp. 819–831, 1993, Publisher: Springer.

[74] S. I. Wright, "A review of automated orientation imaging microscopy(OIM)," *Journal of Computer-Assisted Microscopy(USA)*, vol. 5, no. 3, pp. 207–221, 1993.

[75] M. C. Demirel, B. S. El-Dasher, B. L. Adams, and A. D. Rollett, "Studies on the accuracy of electron backscatter diffraction measurements," in *Electron Backscatter Diffraction in Materials Science*, A. J. Schwartz, M. Kumar, and B. L. Adams, Eds., Boston, MA: Springer US, 2000, pp. 65–74, ISBN: 978-1-4757-3205-4. DOI: 10.1007/978-1-4757-3205-4_6. [Online]. Available: https://doi.org/10.1007/978-1-4757-3205-4_6.

[76] A. D. Rollett, S.-B. Lee, R. Campman, and G. Rohrer, "Three-dimensional characterization of microstructure by electron back-scatter diffraction," *Annual Review of Materials Research*, vol. 37, no. 1, pp. 627–658, 2007, _eprint: https://doi.org/10.1146/annurev.matsci.37.0 DOI: 10.1146/annurev.matsci.37.052506.084401. [Online]. Available: https://doi.org/10.1146/annurev.matsci.37.052506.084401.

[77] S. Lozano-Perez, P. Rodrigo, and L. C. Gontard, "Three-dimensional characterization of stress corrosion cracks," *Journal of Nuclear Materials*, vol. 408, no. 3, pp. 289–295, Jan. 31, 2011, ISSN: 0022-3115. DOI: 10.1016/j.jnucmat.2010.11.068. [Online]. Available: http://www.sciencedirect.com/science/article/pii/S0022311510007762.

[78] F. Bachmann, R. Hielscher, and H. Schaeben, "Grain detection from 2d and 3d EBSD data—specification of the MTEX algorithm," *Ultramicroscopy*, vol. 111, no. 12, pp. 1720–1733, Dec. 1, 2011, ISSN: 0304-3991. DOI: 10.1016/j.ultramic.2011.08.002. [Online]. Available: http://www.sciencedirect.com/science/article/pii/S0304399111001951.

[79] S. Fricke, E. Keim, and J. Schmidt, *Numerical weld modeling — a method for calculating weld-induced residual stresses*, 2-3. Elsevier B.V, 2001, vol. 206, 139–150, ISSN: 0029-5493 Publication Title: Nuclear Engineering and Design. DOI: 10.1016/S0029-5493(00)00414-3.

[80] M. E. Fitzpatrick, A. T. Fry, P. Holdway, F. A. Kandil, J. Shackleton, and L. Suominen. (Sep. 2005). Determination of residual stresses by x-ray diffraction. ISSN: 1368-6550 Issue: 2 Number: 2 Place: Teddington, [Online]. Available: http://eprintspublications.npl.co.uk/2391/.

[81] T. Shoji, Z. Lu, and H. Murakami, "Formulating stress corrosion cracking growth rates by combination of crack tip mechanics and crack tip oxidation kinetics," *Corrosion Science*, vol. 52, no. 3, pp. 769–779, Mar. 1, 2010, ISSN: 0010-938X. DOI: 10.1016/j.corsci.2009.10.041. [Online]. Available: http://www.sciencedirect.com/science/article/pii/S0010938X09005381.

[82] N. Badwe, X. Chen, D. K. Schreiber, M. J. Olszta, N. R. Overman, E. K. Karasz, A. Y. Tse, S. M. Bruemmer, and K. Sieradzki, "Decoupling the role of stress and corrosion in the intergranular cracking of noble-metal alloys," *Nature Materials*, vol. 17, no. 10,

pp. 887–893, Oct. 2018, Publisher: Nature Publishing Group, ISSN: 14764660. DOI: 10.1038/s41563-018-0162-x.

[83] R. Unnikrishnan, K. S. N. S. Idury, T. P. Ismail, A. Bhadauria, S. K. Shekhawat, R. K. Khatirkar, and S. G. Sapate, "Effect of heat input on the microstructure, residual stresses and corrosion resistance of 304l austenitic stainless steel weldments," *Materials Characterization*, vol. 93, pp. 10–23, Jul. 1, 2014, ISSN: 1044-5803. DOI: 10.1016/j.matchar.2014.03.013. [Online]. Available: http://www.sciencedirect.com/science/article/pii/S1044580314000916.

[84] J. B. Cai, C. Yu, R. K. Shiue, and L. W. Tsay, "Stress corrosion cracking of austenitic weld deposits in a salt spray environment," *Journal of Nuclear Materials*, vol. 465, pp. 774–783, Oct. 1, 2015, ISSN: 0022-3115. DOI: 10.1016/j.jnucmat.2015.06.060. [Online]. Available: http://www.sciencedirect.com/science/article/pii/S0022311515300854.

[85] H. Mecking, U. F. Kocks, and C. Hartig, "Taylor factors in materials with many deformation modes," *Scripta Materialia*, vol. 35, no. 4, pp. 465–471, Aug. 15, 1996, ISSN: 1359-6462. DOI: 10.1016/1359-6462(96)00137-6. [Online]. Available: http://www.sciencedirect.com/science/article/pii/1359646296001376.

[86] W. F. Hosford, "The mechanics of crystals and textured polycrystals," *Oxford University Press(USA), 1993,*, p. 248, 1993.

[87] J. Toribio, "Fracture mechanics approach to stress corrosion cracking of pipeline steels: When hydrogen is the circumstance," in *Integrity of Pipelines Transporting Hydrocarbons*, G. Bolzon, T. Boukharouba, G. Gabetta, M. Elboujdaini, and M. Mellas, Eds., ser. NATO Science for Peace and Security Series C: Environmental Security, Dordrecht: Springer Netherlands, 2011, pp. 37–58, ISBN: 978-94-007-0588-3. DOI: 10.1007/978-94-007-0588-3_4.

[88] J. Song and W. A. Curtin, "Atomic mechanism and prediction of hydrogen embrittlement in iron," *Nature Materials*, vol. 12, no. 2, pp. 145–151, Feb. 2013, Publisher: Nature Publishing Group, ISSN: 14761122. DOI: 10.1038/nmat3479.

[89] L. G. Bland and J. S. Locke, "Chemical and electrochemical conditions within stress corrosion and corrosion fatigue cracks," *npj Materials Degradation*, vol. 1, no. 1, pp. 1–8, Dec. 2017, Publisher: Springer Science and Business Media LLC, ISSN: 2397-2106. DOI: 10.1038/s41529-017-0015-0.

[90] D. T. Spencer, M. R. Edwards, M. R. Wenman, C. Tsitsios, G. G. Scatigno, and P. R. Chard-Tuckey, "The initiation and propagation of chloride-induced transgranular stress-corrosion cracking (TGSCC) of 304l austenitic stainless steel under atmospheric conditions," *Corrosion Science*, vol. 88, pp. 76–88, Nov. 1, 2014, ISSN:

0010-938X. DOI: 10.1016/j.corsci.2014.07.017. [Online]. Available: http://www.sciencedirect.com/science/article/pii/S0010938X14003333.

[91] D. D. Macdonald, "The electrochemical nature of stress corrosion cracking," in *Stress Corrosion Cracking of Nickel Based Alloys in Water-Cooled Nuclear Reactors: The Coriou Effect*, Elsevier Inc., Feb. 2016, pp. 239–294, ISBN: 978-0-08-100062-5. DOI: 10.1016/B978-0-08-100049-6.00006-9.

[92] W. F. Flanagan, P. Bastias, and B. D. Lichter, "A theory of transgranular stress-corrosion cracking," *Acta Metallurgica et Materialia*, vol. 39, no. 4, pp. 695–705, Apr. 1, 1991, ISSN: 0956-7151. DOI: 10.1016/0956-7151(91)90138-Q. [Online]. Available: http://www.sciencedirect.com/science/article/pii/095671519190138Q.

[93] A. Pineau, "Crossing grain boundaries in metals by slip bands, cleavage and fatigue cracks," *Philosophical Transactions of the Royal Society A: Mathematical, Physical and Engineering Sciences*, vol. 373, no. 2038, p. 20 140 131, Mar. 28, 2015, Publisher: Royal Society. DOI: 10.1098/rsta.2014.0131. [Online]. Available: https://royalsocietypublishing.org/doi/10.1098/rsta.2014.0131.

[94] T. Zhai, A. J. Wilkinson, and J. W. Martin, "A crystallographic mechanism for fatigue crack propagation through grain boundaries," *Acta Materialia*, vol. 48, no. 20, pp. 4917–4927, Dec. 4, 2000, ISSN: 1359-6454. DOI: 10.1016/S1359-6454(00)00214-7. [Online]. Available: http://www.sciencedirect.com/science/article/pii/S1359645400002147.

[95] J. I. Dickson, D. Groulx, L. Shiqiong, and D. Tromans, "The fractography of stress corrosion cracking of 310 stainless steel: Crystallographic aspects and the influence of the stress intensity factor," *Materials Science and Engineering*, vol. 94, pp. 155–173, C Oct. 1987, Publisher: Elsevier, ISSN: 00255416. DOI: 10.1016/0025-5416(87)90330-2.

[96] T. Tsuru and Y. Shibutani, "Anisotropic effects in elastic and incipient plastic deformation under (001), (110), and (111) nanoindentation of al and cu," *Physical Review B*, vol. 75, no. 3, p. 035 415, Jan. 16, 2007, ISSN: 1098-0121, 1550-235X. DOI: 10.1103/PhysRevB.75.035415. [Online]. Available: https://link.aps.org/doi/10.1103/PhysRevB.75.035415.

[97] W. D. Callister Jr and D. G. Rethwisch, *Materials Science and Engineering: An Introduction 9e Binder Ready Version+ WileyPLUS Registration Card*. John Wiley & Sons, 2012.

[98] P. Peralta and C. Laird, "THE ROLE OF STRAIN COMPATIBILITY IN THE CYCLIC DEFORMATION OF COPPER BICRYSTALS," *Acta Materialia*, vol. 45, no. 7, pp. 3029–3046, Jul. 1, 1997, ISSN: 1359-6454. DOI: 10.1016/S1359-6454(96)

00384-9. [Online]. Available: http://www.sciencedirect.com/science/article/pii/S1359645496003849.

[99] M. A. Linne, T. R. Bieler, and S. Daly, "The effect of microstructure on the relationship between grain boundary sliding and slip transmission in high purity aluminum," *International Journal of Plasticity*, vol. 135, p. 102 818, Dec. 1, 2020, ISSN: 0749-6419. DOI: 10.1016/j.ijplas.2020.102818. [Online]. Available: http://www.sciencedirect.com/science/article/pii/S0749641920300152.

[100] E. A. West, M. D. McMurtrey, Z. Jiao, and G. S. Was, "Role of localized deformation in irradiation-assisted stress corrosion cracking initiation," *Metallurgical and Materials Transactions A*, vol. 43, no. 1, pp. 136–146, Jan. 1, 2012, ISSN: 1543-1940. DOI: 10.1007/s11661-011-0826-5. [Online]. Available: https://doi.org/10.1007/s11661-011-0826-5.

[101] H. I. Khan, N. Zhang, Z. Zhu, D. Jiang, T. Asif, and H. Xu, "Behavior and susceptibility to stress corrosion cracking of a nickel-based alloy in superheated steam and supercritical water," *Materials and Corrosion*, vol. 70, no. 1, pp. 48–56, 2019, _eprint: https://onlinelibrary.wiley.com/doi/pdf/10.1002/maco.201810237, ISSN: 1521-4176. DOI: 10.1002/maco.201810237. [Online]. Available: https://onlinelibrary.wiley.com/doi/abs/10.1002/maco.201810237.

[102] R. W. Staehle and J. A. Gorman, "Quantitative assessment of submodes of stress corrosion cracking on the secondary side of steam generator tubing in pressurized water reactors: Part 1," *Corrosion*, vol. 59, no. 11, Nov. 1, 2003, Publisher: NACE International, ISSN: 0010-9312. [Online]. Available: https://www-onepetro-org.ezproxy.lib.purdue.edu/journal-paper/NACE-03110931.